AGU PUBLICATIONS

JGR

Journal of Geophysical Research: Atmospheres

RESEARCH ARTICLE
10.1002/2015JD024443

Weakening and moistening of the summertime Saharan heat low through convective cold pools from the Atlas Mountains

Robert Redl[1,2], Peter Knippertz[3], and Andreas H. Fink[3]

[1]Institute for Geophysics and Meteorology, University of Cologne, Cologne, Germany, [2]Meteorological Institute, LMU Munich, Munich, Germany, [3]Institute of Meteorology and Climate Research, Karlsruhe Institute of Technology, Karlsruhe, Germany

Key Points:
- Cold pools increase surface pressure by 1–1.5 hPa over multiple days
- About one fifth of column water vapor in affected area originates from evaporation of rain
- Without improved parameterizations, explicitly resolved convection is necessary in model runs

Supporting Information:
- Supporting Information S1

Correspondence to:
R. Redl,
robert.redl@lmu.de

Citation:
Redl, R., P. Knippertz, and A. H. Fink (2016), Weakening and moistening of the summertime Saharan heat low through convective cold pools from the Atlas Mountains, *J. Geophys. Res. Atmos.*, *121*, doi:10.1002/2015JD024443.

Received 3 NOV 2015
Accepted 4 APR 2016
Accepted article online 11 APR 2016

Abstract The West African Monsoon (WAM) and its representation in numerical models is heavily influenced by the Saharan heat low (SHL), a low-pressure system driven by radiative heating over the central Sahara and ventilated by the cold and moist inflow from adjacent oceans. It has recently been shown that a significant part of the southerly moisture flux into the SHL originates from convective cold pools over the Sahel. These density currents driven by evaporation of rain are largely missing in models with parameterized convection. This crucial issue has been hypothesized to contribute to the inability of many climate models to reproduce the variability of the WAM. Observations from the Atlas Mountains, located at the northern flank of the SHL, indicate frequent convection and cold-pool generation during boreal summer, often during episodes of multiple days. This study is the first to analyze impacts of such convective periods on the SHL, based on simulations of two example cases using the Weather Research and Forecast (WRF) model at convection-permitting resolution. Sensitivity experiments with artificially removed cold pools, lower resolutions, and parameterizations are conducted. Results indicate that cold pools lead to increases in surface pressure of more than 1 hPa and significant moisture transports into the desert over several days. This moisture affects radiative heating and thus the energy balance of the SHL. Together with studies focusing on the Sahel, this work emphasizes the need for improved parameterization schemes for deep convection in order to produce more reliable climate projections for the WAM.

1. Introduction

The West African Monsoon (WAM) is a complex system of interactions between ocean, land surface, and atmosphere. Climate models struggle to realistically reproduce the precipitation variability associated with this system [*Hourdin et al.*, 2010]. This is particularly pertinent to the Sahel region (approximately 12°N–20°N), where agricultural productivity, and thus the livelihood of the population, is highly dependent on sufficiently large precipitation amounts. The Sahel was affected by a major drought in the 1970s and 1980s, but rainfall has been recovering since then [*Sanogo et al.*, 2015]. Despite large efforts during the last decade to explain this recovery and to better understand the WAM system, including international research programs and field campaigns such as the African Monsoon Multidisciplinary Analysis (AMMA) [*Redelsperger et al.*, 2006; *Parker et al.*, 2008] and Fennec [*Washington et al.*, 2012], the reasons are still a matter of discussion. The recovery has been attributed to variability in sea surface temperatures [e.g., *Rodriguez-Fonseca et al.*, 2011; *Martin et al.*, 2014], which in turn are affected by aerosols [e.g., *Booth et al.*, 2012], and also to natural [*Evan et al.*, 2015] and anthropogenic [*Dong and Sutton*, 2015] greenhouse gas warming of the Saharan heat low (SHL), a key component of the WAM. An anthropogenic greenhouse gas-related warming and consequent wetting of the Sahel was also found in climate projections for the end of this century [*Vizy et al.*, 2013]. Average surface warming rates over the Sahara are at least 2 times larger than the global mean [*Cook and Vizy*, 2015], but the causes are still disputed [*Lavaysse*, 2015].

During the summer monsoon season, the center of the SHL is typically located over the central Sahara near the border between Algeria and Mali [*Lavaysse et al.*, 2009]. It drives the moist southwesterly monsoon flow across the Guinea Coast toward the Sahel, as well as the dry northerly Harmattan winds across the Sahara [*Parker et al.*, 2005; *Lavaysse et al.*, 2009]. Caused by a lack of operational observations and complex dynamics,

©2016. American Geophysical Union. All Rights Reserved.

the SHL region has been identified as a major source of uncertainty for modeling the WAM [*Agusti-Panareda et al.*, 2010; *Garcia-Carreras et al.*, 2013]. With the Sahara being the most important mineral dust source on Earth, aerosol forcing has received much attention, e.g., during the recent Fennec project [e.g., *Ashpole and Washington*, 2013; *Marsham et al.*, 2013a; *Ryder et al.*, 2013; *Todd et al.*, 2013; *Allen et al.*, 2015]. Uplifted dust is known to have a cooling effect on the surface [*Evan et al.*, 2009], but processes leading to dust emission like monsoon surges or convectively driven cold pools are usually related to an increasing amount of water vapor, which in contrast amplifies radiative heating [*Marsham et al.*, 2015].

Primarily based on the NASA Modern-Era Retrospective Analysis for Research and Applications (MERRA) [*Rienecker et al.*, 2011], *Evan et al.* [2015] suggest that an increasing amount of water vapor in the lower troposphere is responsible for the deepening of the SHL (increase in lower tropospheric temperature) in the past decades. The positive trend in column water vapor (CWV) over the Sahara in MERRA is stronger than in other reanalysis products [*Cook and Vizy*, 2015], which calls the role of the water vapor and the robustness of this result in question [*Cook and Vizy*, 2015; *Lavaysse*, 2015]. The long-term trend in MERRA is influenced by changes in the observation system, e.g., the advent of additional satellite observations during the reanalysis period [*Robertson et al.*, 2011; *Bosilovich et al.*, 2011]. Also, the representation of physical processes relevant for the inflow of moisture into the Sahara is of importance. *Roberts et al.* [2014] attribute day-to-day discrepancies between reanalysis products at the southern fringes of the SHL to convective cold pools. Observations made in 2011 in Bordj Badji Mokhtar (BBM) in southern Algeria [*Garcia-Carreras et al.*, 2013] and a modeling study conducted by *Marsham et al.* [2013b] indicate that a significant part of the meridional moisture flux toward the SHL is caused by convective cold pools created by mesoscale convective systems (MCSs) in the Sahel. The dynamics of these MCSs, typically embedded into African Easterly Waves (AEWs) [e.g., *Fink and Reiner*, 2003], are not captured by global models due to insufficient horizontal resolution and the consequent usage of convective parameterization schemes [*Marsham et al.*, 2013b]. AEWs contribute to the variability of the SHL on the synoptic time scale from the south [e.g., *Couvreux et al.*, 2010; *Lavaysse et al.*, 2010]. From the north, pathways of ventilation for the SHL investigated so far are cold surges from the Mediterranean Sea, often related to midlatitude Rossby waves [e.g., *Knippertz*, 2008; *Vizy and Cook*, 2009, 2014; *Lavaysse et al.*, 2010], and the so-called Atlantic inflow, which is a far inland-reaching sea breeze at the Mauritanian coast [*Grams et al.*, 2010].

Redl et al. [2015] recently presented a new climatology of convection and convective cold pools over the Atlas Mountains, which are located at the northern flank of the SHL. One of their major findings is that convective events over the Atlas Mountains tend to cluster into periods of on average 5day length, often with two strong events on consecutive days. This indicates another possible pathway of SHL ventilation. Such periods were analyzed by *Knippertz et al.* [2009] with respect to dust emission and attributed to synoptic-scale features such as lee cyclones and upper level troughs, but the dynamical consequences for the SHL are so far unknown. During the monsoon months May to September, the Saharan and Tell Atlas Mountains at the border between Morocco and Algeria, as well as the Aurès Mountains in north Algeria and Tunisia (Figure 1b), are most frequently affected by convection and convective cold pools with about six large events per month [*Redl et al.*, 2015, Figures 5 and 6]. One characteristic of cold pools in semiarid environments like northwestern Africa is the associated steep increase in dew point temperature (T_d) at the surface [e.g., *Knippertz et al.*, 2007; *Engerer et al.*, 2008; *Emmel et al.*, 2010]. Comparing this variable measured at manned synoptic and automated weather stations (AWSs) with the operational analysis of the European Centre for Medium-Range Weather Forecasts (ECMWF) indicates that issues with parameterized convection, as known from the Sahel region, affect Northwest Africa in a very similar way (Figures 2a–2c). Biases during the winter months are small in magnitude and do not show a systematic geographical distribution (Figure 2a). On the contrary, in summer biases are predominantly negative reaching values well below −3 K, particularly along the southern foothills of the Atlas chain, where the effects of cold pools are felt most significantly (Figure 2b). Monthly time series show a continuous increase in the negative bias of dew point temperature toward the summer months, with the largest magnitudes in July and August (Figure 2c), concomitant with the peak in cold-pool activity [*Redl et al.*, 2015]. Looking at individual cases and stations reveals an interesting mix of satisfactory reproduction in both ECMWF operational analysis and ERA-Interim reanalysis (Figures S1a–S1c in the supporting information), missed events (Figures S1d and S1e), and large discrepancies between the two analysis products (Figure S1f). The AWS shown in Figure 1b and used in Figure S1 were not assimilated into the two analysis products. As both use the same synoptic stations for data assimilation, causes for differences are likely related to the assimilation of remote sensing data, the different horizontal resolution, and changes in model physics. However, a detailed analysis of these differences is beyond the scope of this paper.

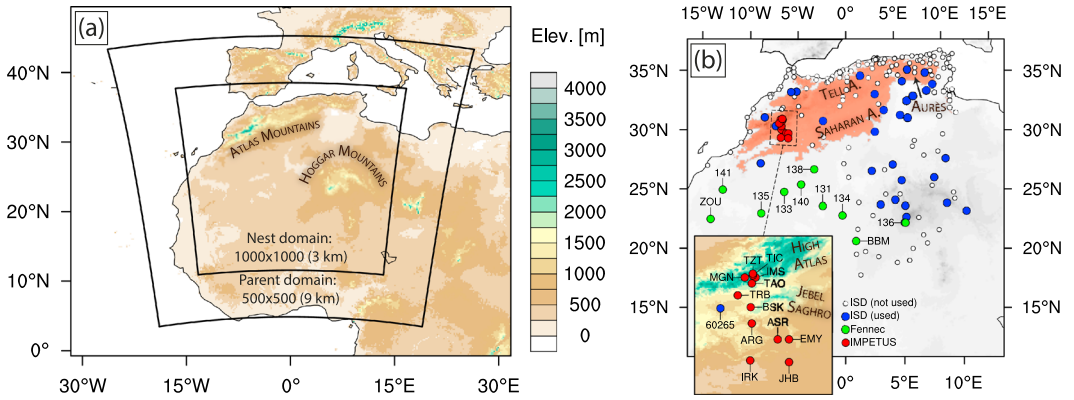


Figure 1. Model domain, location of ground observations, and important geographical names. (a) Model parent and nest domains with orography. (b) Nest domain including the locations of ground observations from the data sets ISD, Fennec, and IMPETUS. The red shading indicates grid points over the Atlas Mountains with an elevation of more than 500 m.

The present study exploits the unique coexistence of two AWS networks at the Saharan foothills of the High Atlas Mountains and the western Sahara in 2011 and 2012. Two convective periods in June 2011 and 2012, identified by *Redl et al.* [2015], are simulated using the Weather Research and Forecast (WRF) model with a horizontal resolution of 3 km, which enables to explicitly resolve convection. In both cases cold pools with a horizontal extent of several hundred kilometers are observed in satellite imagery. The aim of this study is to assess the mesoscale to synoptic-scale direct impacts of such systems on surface pressure, moisture transport, and surface radiation balance in the northern SHL region. In addition, the influence of a reduction of horizontal resolution and the usage of parameterized convection is analyzed for one of the events to illustrate the possible effects in climate simulations.

Section 2 presents the boundary conditions used to drive WRF and details the observations used for the model evaluation. The model configuration and the experimental setup are described in section 3. Results, including a description of the synoptic situation during the selected cases, are presented in section 4, followed by a discussion in section 5. Supporting information referred to in the text are available online.

2. Data

2.1. Meteosat SEVIRI "Desert Dust" Product

The Spinning Enhanced Visible and InfraRed Imager (SEVIRI) on board the second-generation Meteosat (MSG) satellites is a line-by-line scanning passive radiometer with three visible, one near-infrared, and eight thermal infrared channels. It has a spatiotemporal resolution of 15 min and 3 km at nadir. *Lensky and Rosenfeld* [2008] describe a number of useful red-green-blue composites, including the "desert dust" product employed here. In this product, the difference in brightness temperatures measured by the 12.0 and 10.8 μm channels ($BTD_{12.0-10.8}$), which indicates the opacity of clouds, is mapped to red. $BTD_{10.8-8.7}$ is mapped to green; the 8.7 μm channel is sensitive to the size of quartz mineral particles. The brightness temperature in the 10.8 μm window channel indicates cloud top and surface temperature and is mapped to blue. The desert dust images

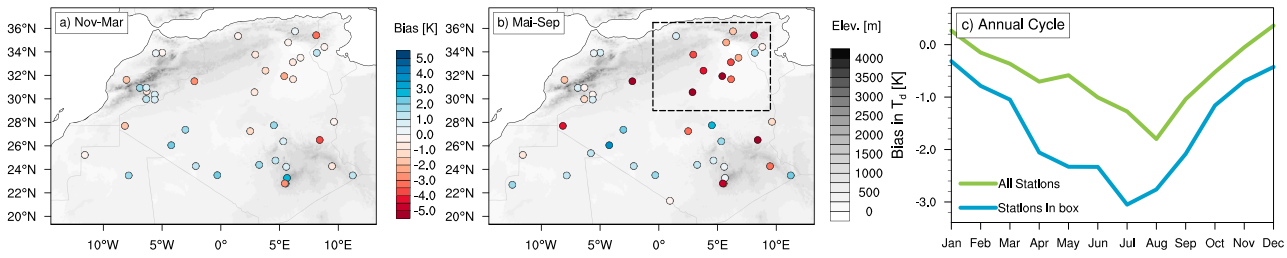


Figure 2. Bias in 2 m dew point temperature T_d in ECMWF operational analysis with regard to ground observations. (a) Average bias per station for the months November–March for 2011–2012. (b) As in Figure 2a but for the months May–September, the dashed box indicates an area frequently affected by cold-pool events. (c) Annual cycle of the bias averaged over all stations and over the stations located in the dashed box from Figure 2b.

are used in section 4 to illustrate the evolution of selected cold-pool events similar to, e.g., *Marsham et al.* [2013a], *Allen et al.* [2013], and *Bou Karam et al.* [2014]. In the absence of higher-level clouds, cold pools are visible due to dust uplift by pinkish colors (labeled A and B in Figure 4b). Clouds with a large vertical extent appear in red labeled (C) and thin cirrus clouds in black labeled (D) in Figure 4b. Increased CWV can hinder the detection of uplifted dust [*Brindley et al.*, 2012].

2.2. Surface Observations

Satellite images provide valuable information on cold pools, but details about their meteorological characteristics can only be obtained from surface observations. Three sources are used in this study with locations shown in Figure 1b: (1) surface synoptic observations (SYNOP) (FM-12) and aerodrome routine meteorological reports (METAR) (FM-15) reports from manned weather stations and airports [*World Meteorological Organization*, 2010] obtained from the quality controlled National Climatic Data Center (NCDC) Integrated Surface Database (ISD) [*Smith et al.*, 2011]. (2) Automated weather stations (AWSs) installed and operated by the IMPETUS (An Integrated Approach to the Efficient Management of Scarce Water Resources in West Africa) project [*Speth et al.*, 2010] in southern Morocco between 2001 and 2010 and extended through the Fennec Intensive Observation Periods (IOPs) in June 2011 and 2012 by the project titled "Multi-scale subtropical controls on the position and intensity of the summertime West African heat low," which was funded by the German Science Foundation (DFG) and which is associated with the UK and French Fennec initiatives. The network is located in the basins of the rivers Dadès and Drâa and includes mountain stations in the High Atlas and Jebel Saghro. It was initially deployed in 2001 with 12 stations, but for the cases investigated here only data from 8 (6) stations are available for 2011 (2012). The stations were deinstalled in September 2012. Measured quantities are air temperature and humidity, soil temperature and humidity, global and net radiation, wind speed and direction, and precipitation. (3) The stations network installed and maintained by the UK Fennec project in Algeria and Mauritania [*Hobby et al.*, 2013], which includes two supersites, Zouérat (ZOU) in Mauritania and Bordj Badji Mokhtar (BBM) in Algeria, as well as eight additional AWSs. Details about the full instrumentation of the supersites can be found in *Marsham et al.* [2013a] and *Todd et al.* [2013]. Here only measurements of air temperature and humidity, upwelling and downwelling short- and long-wave radiation, and pressure are used. For the 2012 case, data from all stations but the supersite Zouérat, which was not operated in 2012, are available. Due to technical issues, only data from six stations are available for the 2011 case. The Fennec network ceased operations in 2013.

2.3. ECMWF (Re)-Analysis

The operational analysis of the ECMWF with 6-hourly temporal resolution serves as initial and boundary condition for all WRF model runs. Data for the first (second) case in 2011 (2012) are from model version 37r2 (38r1). Changes between these versions include the assimilation of additional satellite data and an updated convection scheme. Horizontal resolution is T1279 (approximately 0.14°) with 91 vertical layers. In addition to the operational analysis, the ERA-Interim reanalysis [*Dee et al.*, 2011] is included for comparison in Figures 5, 7, and S1. ERA-Interim is created with the version 31r2 of the operational model and updated regularly. The horizontal resolution is T255 (approximately 0.75°) with 60 vertical layers up to 0.1 hPa. Fennec and IMPETUS data were not assimilated, but the ECMWF 4D-Var system assimilates pressure and daytime humidity from practically all SYNOP stations in the region, both for ERA-Interim and operational analysis. SYNOP temperature and humidity are used in the surface analysis only.

3. Model Description and Case Selection

All sensitivity experiments are designed as a comparison between an undisturbed control run with a realistic convective cold pool and modified runs. These include "unphysical" changes to the treatment of latent heating and cooling, as well as the usage of convection parameterization schemes. All experiments were carried out with the WRF model version 3.5.1 with the Advanced Research WRF (ARW-WRF) dynamical core [*Skamarock et al.*, 2008].

3.1. Model Setup for Control Runs

Even though the focus of this study is on cold-pool events originating from the Atlas Mountains, the model domain covers a much larger region in order to have a realistic representation of the SHL. The model domain is centered at 25°N and 0°E, the climatological center of the SHL in June and July [*Lavaysse et al.*, 2009]. A two-way nesting is used with a horizontal resolution in the parent domain of 0.081° (approximately 9 km), which covers the western part of the African continent and parts of southern Europe (Figure 1a). The nest

domain has a horizontal resolution of 0.027° (approximately 3 km), covers the SHL, the Atlas and Hoggar Mountains, and extends far enough south to include MCSs at the southern flank of the SHL. Two-way nesting was selected as it enables feedback from the nest to the parent domain. Modifications to the pressure gradient at the fringes of the SHL, e.g., caused by cold-pool events located inside the nest domain, can in such a setup influence the atmospheric flow in the parent domain, which in turn may alter the ventilation of the SHL. A one-way nesting without feedback from the nest domain would break this coupling, with negative consequences for the interpretability of the experiments. In the vertical, 70 layers are used, 20 of them below $\eta = 0.8$ (about 1.8 km above ground; η is the terrain-following vertical coordinate of WRF). The number of layers in the planetary boundary layer (PBL) is usually fixed in WRF with 11 layers below $\eta = 0.8$ and independent of the total number of layers. Increasing this number has been shown to have a positive effect on other PBL phenomena such as the nighttime low-level jet (NLLJ) and low-cloud formation over southern West Africa [*Schuster et al.*, 2013]. The selection of parameterization schemes is consistent with this study: Mellor-Yamada-Nakanishi-Niino level 2.5 (MYNN2) for the PBL; the Noah land surface model; the Morrison double moment (MOR2) microphysics scheme; the Rapid Radiative Transfer Model for GCMs (RRTMG) for short- and long-wave radiation; the Grell-3d convection scheme (only used in parent domain). References to all parameterization can be found in the WRF User Guide [*Wang et al.*, 2013].

3.2. Model Modifications for Sensitivity Experiments

To quantify the impact of large-scale convectively driven cold pools from the Atlas Mountains on the SHL, it is necessary to remove them from the model. The most drastic way is to suppress latent heat (LH) release over the entire domain. This approach, however, also suppresses convection in the Sahel and therefore makes it difficult to separate the effect of Atlas convection on the SHL. Consequently, we decided to restrict manipulations to the model microphysics to elevated terrain in Morocco, Algeria, and Tunisia (defined by a threshold for the elevation of 500 m, red area in Figure 1b), where the bulk of convection north of the SHL occurs [*Redl et al.*, 2015]. In a first experiment, latent heating and cooling were suppressed completely, resulting in removal of convection and associated cold pools in the Atlas region. The problem with this approach is that removing the whole convective system means that the upper level flow is significantly changed (Figure S4d). The upward transport of mass and the anticyclonic outflow at the tropopause are missing. Consequently, the difference in surface pressure between control run and experiment are not solely caused by the removal of cold pools. Also, we found that for one test case (first two days of the case described in section 4.1) the moisture, not precipitating out over the Atlas Mountains, is transported westward and triggers convection outside of the modified area 1 day later. Experiments spanning multiple days are therefore difficult to interpret.

Given the temporal clustering of convection, however, experiments over several days are desirable. Thus, a second experiment was designed to remove the cold pool while keeping the convective system itself as intact as possible. A main driver for the cold pool is the evaporation of raindrops on their way from the cloud to the surface. The idea behind this experiment is therefore to disable the evaporative cooling (LH <0) below cloud base. In addition, the water vapor created by evaporation (ΔQ_{vapor}) below cloud base is removed. This experiment did not disturb the upper level flow significantly (Figure S4e), but the cold pool was also only partially removed (cf. Figures S4a and S4b). This experiment is therefore well suited to investigate the amount of rain evaporated below cloud base, but the total effect of the cold pool remains unclear.

To overcome this issue, vertical profiles of latent heating and mixing ratios of all hydrometeors were calculated from the control run of the test case. Profiles from grid points over the Atlas Mountains, where rain reached the surface at 18 UTC (5006 profiles in total) were selected, moved into a common origin relative to their respective cloud bases, and then averaged. The maximum evaporative cooling was found about four model layers above cloud base (Figure 3a). According to the profiles of the mixing ratios for rain (Q_{rain}), graupel ($Q_{graupel}$), and snow (Q_{snow}), this is not where the strongest evaporation of rain is found but where snow and graupel melts to rain. This is supported by *Engerer et al.* [2008], who found ice processes to be particularly important for the strength of a cold pool. Thus, the explanation for the incomplete removal of the cold pool in the second experiment is that a significant fraction of cooling remained in the system (Figure 3b).

Therefore, a third experiment was created. Again, modifications are only applied to the grid points over the Atlas Mountains, but this time evaporative cooling and ΔQ_{vapor} were set to 0 for grid cells with $Q_{rain} > 0$ and LH < 0. This effectively removes all cooling from the system (Figure 3c), but the release of LH remains largely unchanged. As a result, the upper part of the convective systems develops in a way comparable to the control

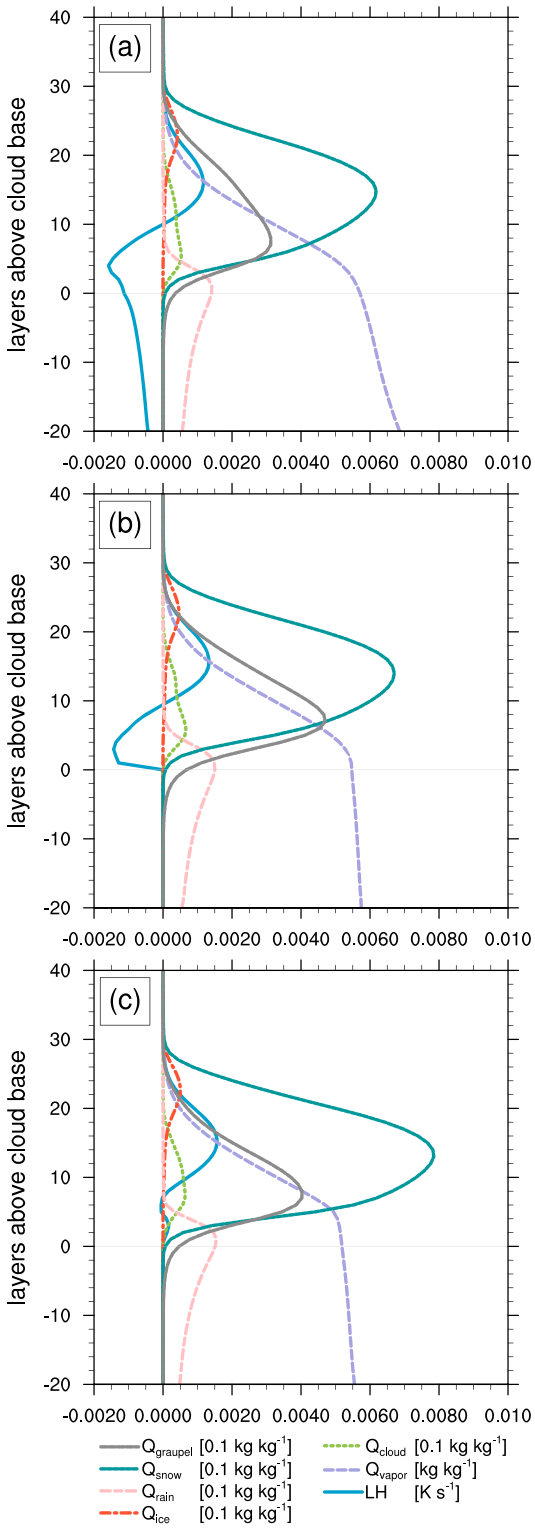


Figure 3. Average vertical profiles of latent heating/cooling as well as mixing ratios for all hydrometeor species in the used microphysics scheme. Profiles are calculated by selecting grid points where rain reaches the surface over the Atlas Mountains at 18 UTC and aligning these profiles to their cloud base. (a) Control run, (b) no LH below cloud base, and (c) no evaporative cooling at grid cells with rain.

run (Figure S4f), while the cold pool is removed (Figure S4c). All further experiments are carried out with this model configuration.

3.3. Tracing of Moisture From Evaporation of Rain

In addition to running sensitivity experiments with removed cold pools, a tracer variable for water vapor created by the evaporation of rain (Q_{ev}) is introduced to WRF and used in the control runs. For each time step, the tendencies in water vapor created from the microphysics scheme (ΔQ_{vapor}) are added to this new tracer variable.

$$Q_{ev}(t) = Q_{ev}(t-1) + \Delta Q_{vapor} \tag{1}$$

This is only done for grid points located over the Atlas Mountains with LH <0, $Q_{rain} >0$, and $\Delta Q_{vapor} >0$. The new tracer is then advected with the model winds. To get a realistic estimation how far this moisture can be transported, account is also taken for the "consumption" of moisture by the creation of new cloud drops or other microphysical processes over the whole domain, also away from the Atlas Mountains. For grid points with $\Delta Q_{vapor} < 0$ the tracer is then reduced:

$$Q_{ev}(t) = Q_{ev}(t-1) - \min(Q_{ev}(t-1), -\Delta Q_{vapor}) \tag{2}$$

Cycles of consumption and recreation away from the Atlas are not taken into account; e.g., if the moisture from the tracer is used to create a new cloud and possibly rain drops outside the Atlas Mountains domain delineated in Figure 1b, then the moisture from the evaporation of these drops is not fed back into the tracer. Thus, the tracer variable introduced here yields a conservative estimation of the effect of moisture created by cold pools. Finally, the tracer variable is enabled in both WRF domains, but values from the parent domain are overridden by the child domain in overlapping areas due to the usage of two-way nesting.

3.4. Selection of Cases for Sensitivity Experiments

Cases for the sensitivity experiments were selected based on the cold-pool climatology presented in *Redl et al.* [2015]. A basic condition was that the IMPETUS and Fennec stations are available for model evaluation, which restricts the time span to the years 2011 and 2012. The climatology for the IMPETUS stations (red dots in Figure 1b) contains 12 cases for 2011 and 7 cases for 2012. The selection was further limited by a screening of Meteosat SEVIRI desert dust images. In order to enable a direct comparison between model output and satellite images, only cases where the leading edge of the cold pool was not covered by high-level clouds were selected. Control runs with WRF were created for the remaining eight cases. In two of them, the cold pool in the first night developed in satisfactory agreement with the satellite observations. Details of these two cases are discussed in sections 4.1 and 4.2. Both cases are of medium or even below medium intensity. Accordingly, estimates of the impacts are rather conservative. The representativeness is discussed in more detail in the supporting information (Text S1).

3.5. Low-Resolution Experiments With Different Convection Schemes

It has been shown that deep convection over the Sahel is responsible for a significant part of the monsoonal northward moisture flux and that parameterized convection leads to a significant bias not only in transport of moisture but also in geopotential height in the Sahel region [*Marsham et al.*, 2013b]. These conclusions were drawn from comparison between runs using the UK Met Office Unified Model (UM) with parameterized and explicitly resolved deep convection at horizontal resolutions of 4 and 12 km. It is not clear whether these conclusions are robust for other convection schemes and coarser horizontal resolutions. Also, the Atlas Mountains at the northern flank of the SHL were not part of the model domain. Regional climate simulations for Africa are currently performed with horizontal resolutions of 25 to 50 km (0.22° to 0.44°) [e.g., *Jones et al.*, 2011]. Therefore, for the first case study additional model runs using horizontal resolutions of 0.22°, 0.44°, and 0.75° were carried out with eight different parameterization schemes for deep convection, but otherwise configurations were identical to the parent domain of the control run (Table 1).

4. Results

This section begins with descriptions of the two cases including their reproduction by the WRF model (sections 4.1 and 4.2), followed by a discussion of the influence on surface pressure (section 4.3), moisture transport (section 4.4), and radiation (section 4.5). Finally, results are compared with low-resolution model runs (section 4.6).

Table 1. Parameterization Schemes for Deep Convection Used in Low-Resolution Experiments[a]

WRF Namelist	Abbreviation	Scheme
1	KF	Kain-Fritsch
2	BMJ	Betts-Miller-Janjic
3	GF	Grell-Freitas
4	OSAS	Old Simplified Arakawa-Schubert
5	G3	Grell-3D
6	Tiedtke	Tiedtke
7	ZMF	Zhang-McFarlane
14	NSAS	New Simplified Arakawa-Schubert

[a] References can be found in *Wang et al.* [2013].

4.1. Description of Case 1: 2011-06-20 to 2011-06-24

The selected days are part of a convectively active period in the second half of June 2011 and fell into the 2011 aircraft IOP of the Fennec project. In this period convection over the Atlas Mountains was detected on 10 consecutive days by microwave satellites [*Redl et al.*, 2015, Figure 7]. The strongest convective cold-pool event was observed in the middle of this period on 20 June. This day was selected as the start date of the model run in order to reproduce this major event as close to reality as possible.

The synoptic situation preceding this convective event with an unusual westerly location of the SHL [*Engelstaedter et al.*, 2015] and northward transport of midlevel moisture, which supports convection over the Atlas Mountains [*Knippertz et al.*, 2003], is discussed in the supporting information (Text S2). The model run for this episode is initialized on 20 June, 00 UTC, and integrated over 96 h until 24 June, 00 UTC. Each 00 UTC time step in this period is shown in Figure 4. On the first simulation day convection is evident over the Atlas Mountains in both the model and satellite observations between 12 and 13 UTC. The development begins with individual cells, and the corresponding cold pools merge during the following hours. At 18:15 UTC the system has already formed one merged cold pool with a southward moving leading edge reaching from approximately 9°W to 2°E. At this time, high-level clouds cover large parts of the cold pool, such that it is only visible by the arc-shaped edge of the clouds in Figure 5b. Some individual cells are located close to the IMPETUS station network. Satellite images (Figures 5b and 5d) indicate that the stations were not hit by the connected southward moving part of the cold pool but by smaller individual cold pools covered by high-level clouds. The time shift between cold-pool detection at the stations IRK (Figure 5a) and JHB (Figure 5c) and the increase in T_d in WRF at the same locations indicate that WRF is not able to reproduce the individual cells in strength and position. This inability could be related to spin-up effects or the overall stochastic nature of convection, but this aspect was not further investigated. However, at 00 UTC the connected large cold pool, well visible in 2 m T_d from WRF (Figure 4c, label E), matches the satellite observation in position and propagation speed reasonably well (Figure 4b, label A). At this time, Fennec AWS 138 was hit by the leading edge (Figures 5e and 5f). T_d at this station increased by about 9K. In WRF the cold pool arrives delayed by about 1 h, leading to an increase in T_d of about 8 K. This indicates that WRF reproduces the overall characteristics of the event but with a slightly weaker cold pool.

The ECMWF operational analysis, which is used to drive WRF, only partially reproduces the cold pool (Figure 5e). Compared to measurements at IRK and JHB, the analysis is too dry by up to 4 K in T_d between 12 and 15 UTC (Figures 5a and 5c). As one might expect from the weaker cold pool in WRF, the model is also too dry during this time.

On the second simulation day a somewhat smaller convective system forms over the Saharan and Tell Atlas Mountains at the border between Morocco and Algeria (Figure 4e, label F). This event is also visible in 2 m T_d from WRF (Figure 4f, label H) but with a less clear-cut leading edge. For the same day, satellite imagery shows a large cold pool formed in the central Sahara at about 23°N (Figure 4e, label G). WRF reproduces this event but too far south (Figure 4f, label I). With increasing integration time, deviations to the analysis grow with some significant displacements of convective systems and contours of geopotential height in the last two integration days (Figures 4g–4l).

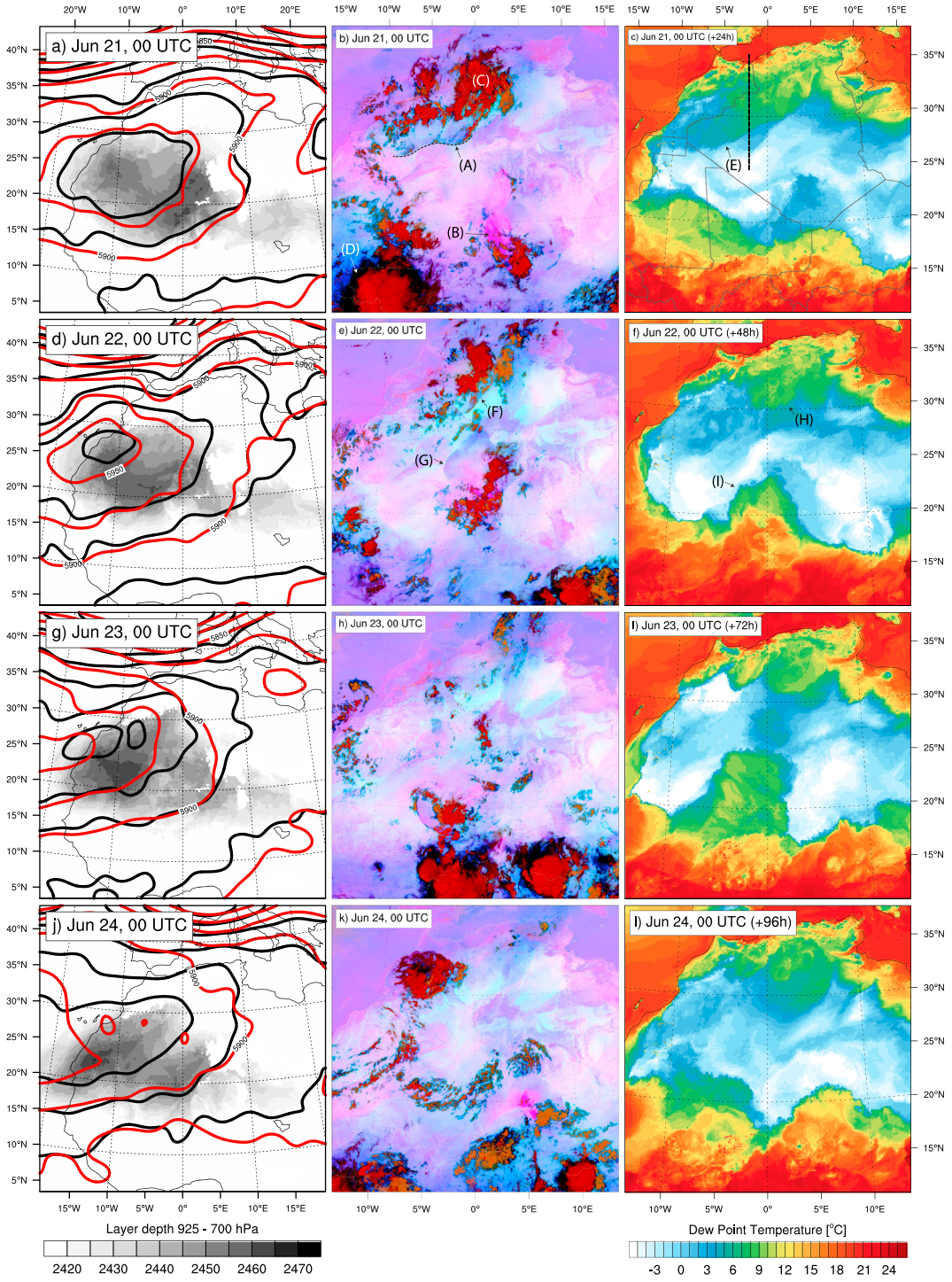


Figure 4. Evolution of case 1. (a, d, g, j) Geopotential height at 300 hPa from WRF (black lines) and ECMWF operational analysis (red lines) together with layer depth between 925 and 700 hPa from WRF (shading). (b, e, h, k) Meteosat SEVIRI desert dust product. (c, f, i, l) The 2 m dew point temperature from WRF. Figures 4a–4c: initialization time +24 h, Figures 4j–4l: initialization time +96 h. The bold dashed line in Figure 4c indicates the location of the cross section shown in Figure 12.

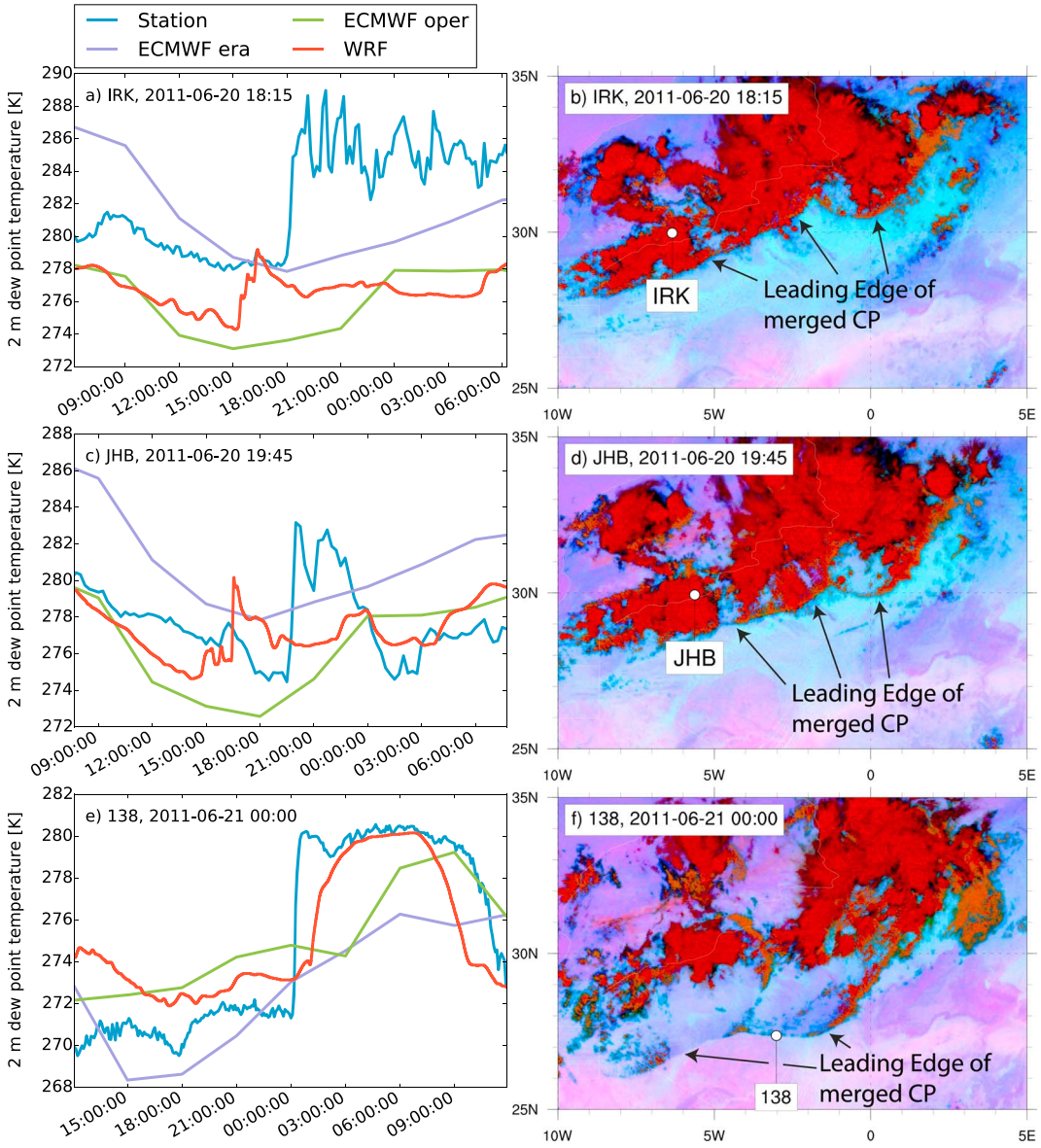


Figure 5. Passage of the leading edge of cold pools at ground stations during the first simulation day of case 1. (a, c, e) The 2 m observation of dew point with simulated values from WRF, ERA-Interim, and ECMWF operational analysis. (b, d, f) Time of the passage in Meteosat SEVIRI desert dust product with respective station locations marked. Station numbers and abbreviations are shown in Figure 1b.

4.2. Description of case 2: 2012-06-27 to 2012-07-01

Like the first case, the selected days are also part of a longer convectively active period [*Redl et al.*, 2015, Figure 7]. For the start date of 27 June, microwave images do not indicate the strongest convective activity during this period, but a very clear cold pool is evident in IR images.

The situation leading up to this case is again discussed in the supporting information (Text S3). The model run for this episode was initiated on 27 June at 00 UTC and integrated over 96 h until 1 July, 00 UTC. The evolution of the simulation during the whole period is shown in Figure 6. As in the first case, the development of new convective cells over the Atlas Mountains starts on the first day between 12 and 13 UTC. This time, however, the cells are more scattered throughout the region. Nevertheless, cold pools of individual cells merge again to build one large system. Unfortunately, this is less visible on IR satellite images (Figures 7b, 7d, and 7f). At 20 UTC the synoptic station of Bechar (Algeria, 60571) reports a steep increase in T_d of about 6 K, indicating the arrival of the cold pool (Figure 7a). WRF also shows an increase in T_d at this location but delayed by about

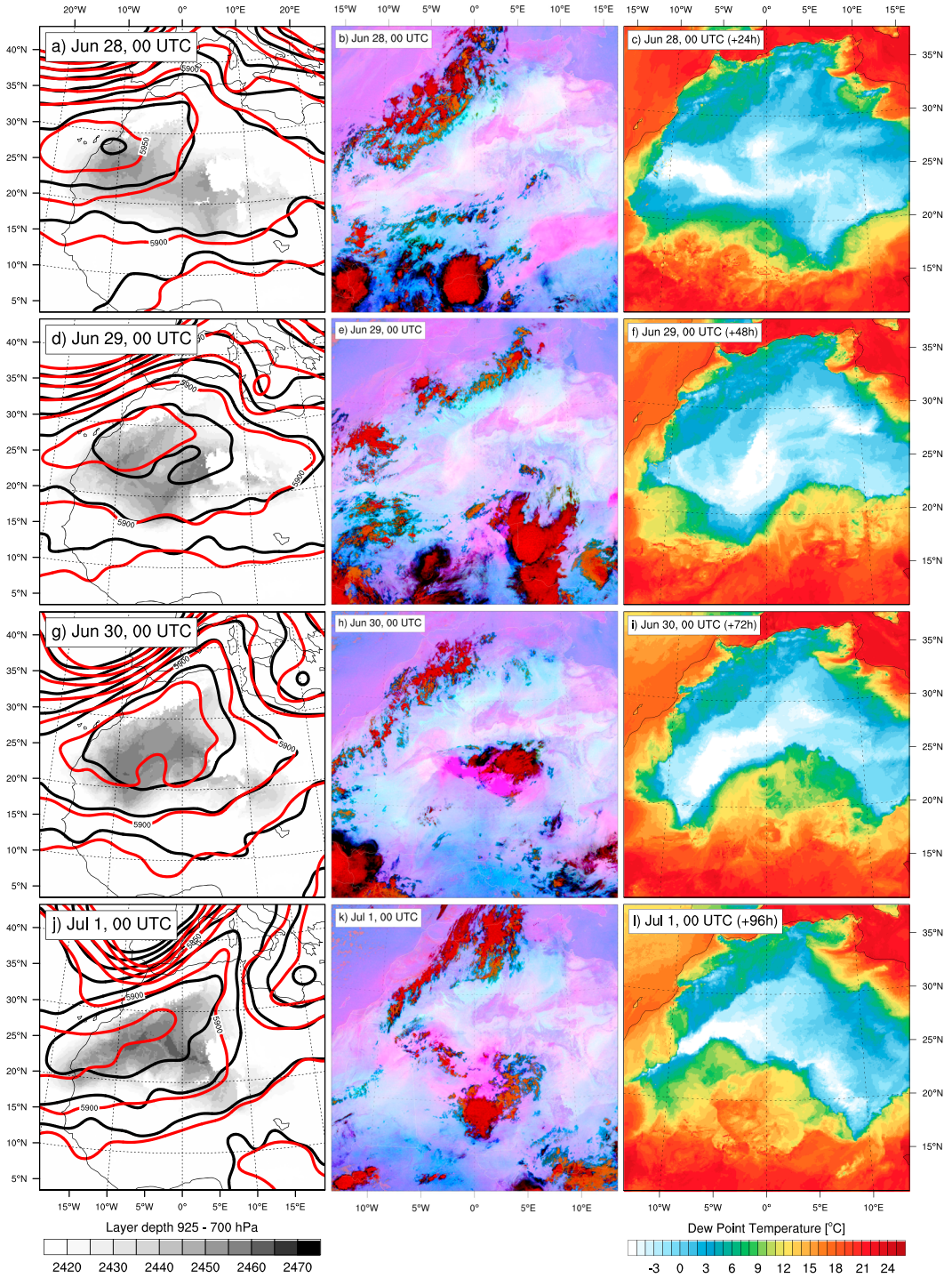


Figure 6. Evolution of case 2, as in Figure 4.

1 h and weaker. Also, it is worthy of note that WRF has a significant dry bias compared to the observation of about 7 K before the event and 10 K afterward, most likely related to but not fully explained by the dry bias in the driving ECMWF analysis. At 22 UTC a cold pool reaches the synoptic station of Tindouf (Algeria, 60565) (Figures 7c and 7d). Again, WRF shows a significant dry bias there of about 6 K before the event, but the timing is almost perfect. Later at about 01 UTC the Fennec AWS 141 is reached by the merged cold pool (Figures 7e and 7f). The observed increase in T_d of about 10 K is reproduced by WRF, although not with a perfect timing. In the corresponding IR satellite image (Figure 7f) the leading edge of the cold pool is hardly visible close to

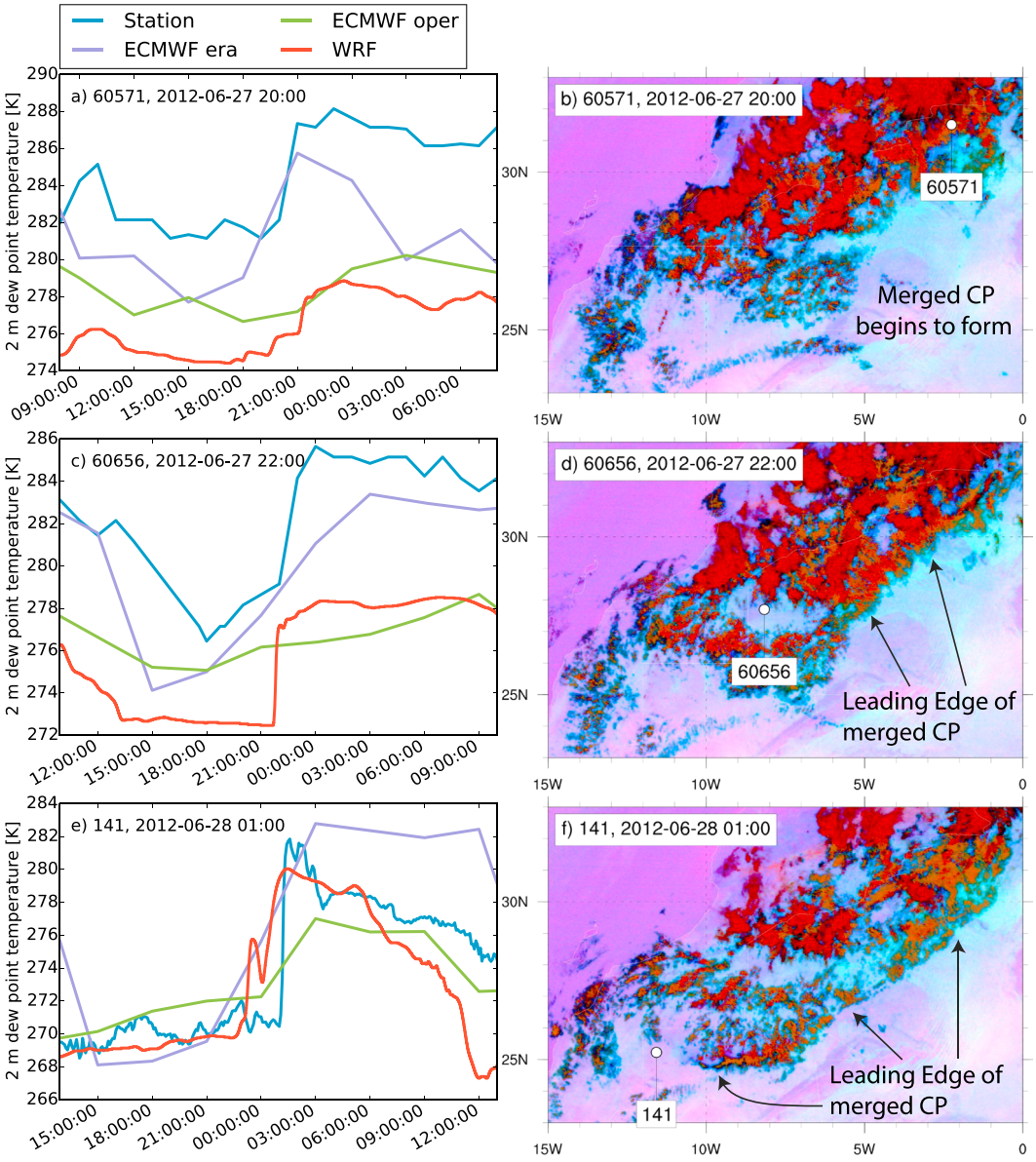


Figure 7. Passage of the leading edge of cold pools at ground stations for the first simulation day of case 2, as in Figure 5.

the station, possibly due to high levels of CWV as discussed in *Brindley et al.* [2012], but the arc-shaped clouds to the east of the station indicate its position.

As in the first case, the ECMWF analysis partially reproduces the cold pool (Figure 7e) but compared to observations is much less pronounced. Interestingly ERA-Interim, which is included for comparison in Figures 5 and 7, reproduces the increase in T_d better than the operational analysis. The differences between analysis and reanalysis demonstrate the difficulty to simulate these events, especially in data-sparse regions like Northwest Africa. The higher resolved analysis is not always outperforming the reanalysis, which indicates that differences are not solely explainable by the horizontal resolution.

In the following days, the ridge moved farther eastward, which brought the subsequent trough closer to the Moroccan coast, as is well reproduced by WRF. Even after 96 integration hours, the deviation of WRF's 500 hPa geopotential field from the analysis remains small (Figures 6a, 6d, 6g, and 6j). Convection over the Atlas Mountains reaching from West Sahara/south Morocco to north Algeria is observed during all simulated days and well reproduced by WRF (Figures 6b, 6c, 6e, 6f, 6h, 6i, 6k, and 6l).

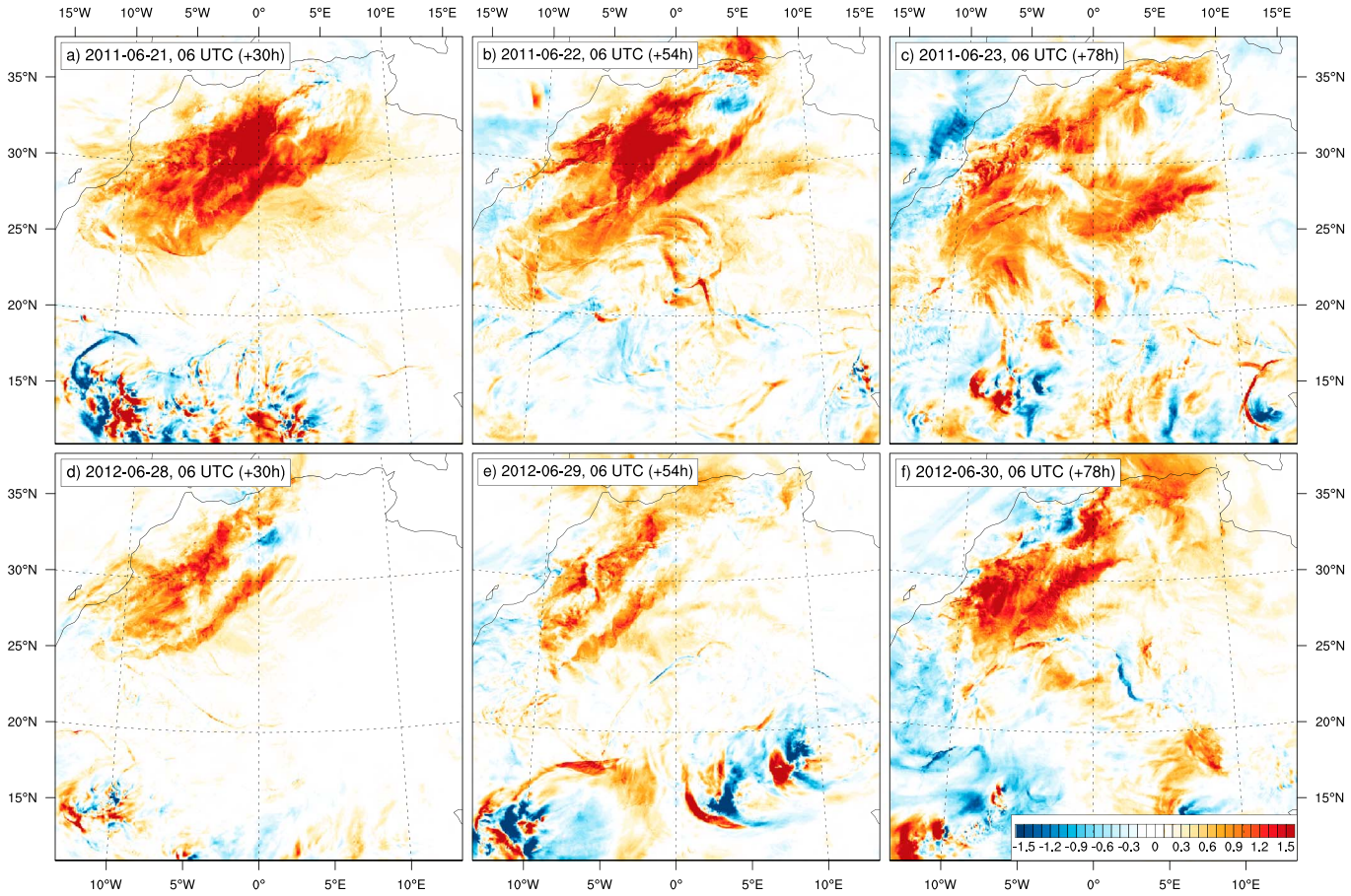


Figure 8. Difference in MSLP between the control and the no-cold-pool runs in hectopascals. (a–c) Case 2011-06-20 and (d–f) case 2012-06-27.

4.3. Impact on Surface Pressure

The two cases described above are used to illustrate impacts of the cold pools on the SHL. In both cases the propagation of the cold pools is directed from the Atlas Mountains toward the SHL. Their leading edge becomes visible in a reduction of the layer depth between 925 and 700 hPa (Figures 4a, 4d, 4g, 4j, 6a, 6d, 6g, and 6j; differences are shown in Figure S7), which is often used as an indicator for the SHL position, strength, and extent [e.g., *Lavaysse et al.*, 2009]. The layer depth is closely related to the surface pressure (P_{sfc}), which is analyzed here using differences between the control and no-cold-pool runs (section 3.2, third experiment).

The most pronounced effect in P_{sfc} is visible in the morning hours after the cold-pool event, before the air gets heated by solar radiation and mixes vertically. All 06 UTC dates from both cases are shown in Figure 8. For case 1, the first morning shows the largest effect (Figure 8a). Excluding grid cells south of 20°N, an increase of at least 1 hPa (1.5 hPa) is found over an area of approximately 580,000 km^2 (186,000 km^2) (for comparison, Morocco without Western Sahara has a size of 446,550 km^2). The second case starts with a weaker increase in P_{sfc}, but the consecutive convective events produce an increase of at least 1 hPa over an area of approximately 392,000 km^2 on the third day (Figure 8f). Relative to the pressure difference between the southern foothills of the Atlas Mountains and the SHL core of about 5–6 hPa (Figures S5 and S6), the magnitude of the cold-pool-induced changes are substantial. That means that the pressure gradient is increased by up to one third over a period lasting several days, which must alter the ventilation of the SHL. However, a direct effect on the SHL core around 20°N during the considered time period is not found in either of two cases. To analyze how long it takes the SHL to react to the cold-pool influence, the integrations were extended by two additional days. During these days, the impact of Atlas convection on the heat low in terms of surface pressure increase slowly spreads in time and magnitude across the core region of the heat low (supporting information Figure S8). Thus, the WRF simulations suggest that successive cold-pool occurrence from the Atlas Mountains integrate to a discernible weakening of the West Saharan heat low. Given the regularity of these events, it can

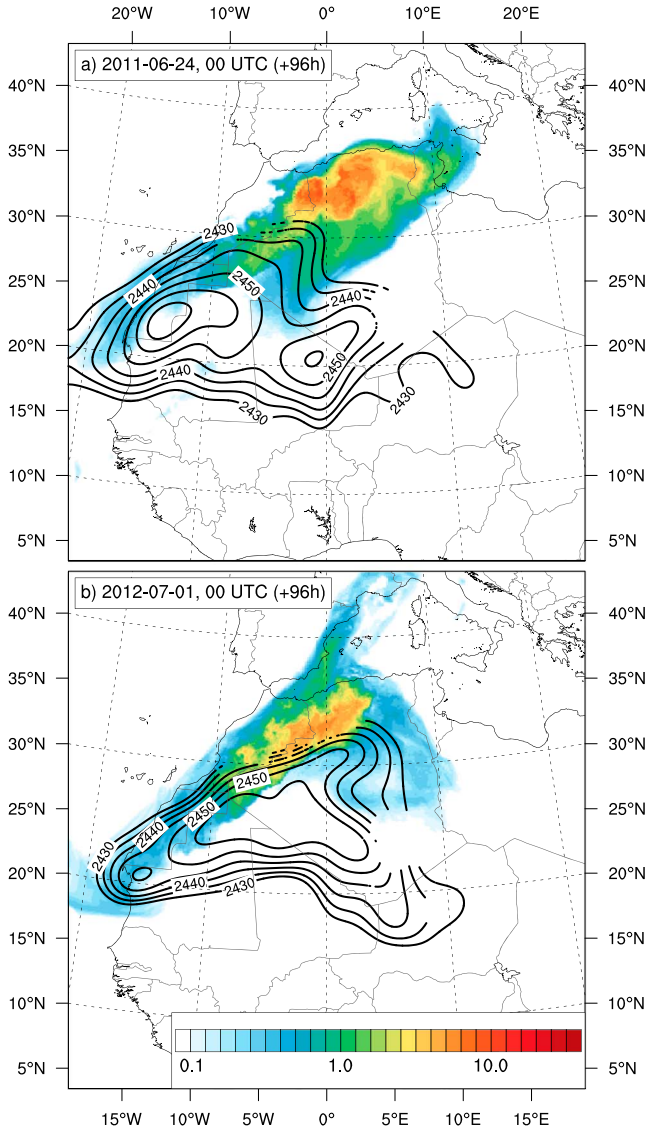


Figure 9. Vertical integrated water vapor created by evaporation of rain at the end of the control runs in kg m^{-2}. (a) Case 1 and (b) case 2. The position of the heat low is indicated by 500 km low-pass-filtered layer depth between 700 and 925 hPa (black lines, in geopotential meters).

be expected that an insufficient representation of these events in a model can create a biased mean state of the SHL.

4.4. Cold Pools as Moisture Source for the Desert

Cold pools generated from MCSs in the Sahel account for nearly one third of the meridional moisture flux toward the SHL [*Garcia-Carreras et al.*, 2013]. Here the accumulated contribution of the cold pools originating from the Atlas Mountains during both case studies is calculated using the tracer variable Q_{ev} introduced in section 3.3.

During the whole 96 h time period evaporation of rain over the Atlas Mountains is added and consumption by condensation is removed from Q_{ev}. The results for the end of both cases are shown vertically integrated in Figure 9. For the first case study Q_{ev} shows larger values, consistent with the larger signal in surface pressure. Maximum values over north Algeria originate from fresh cold pools on the last simulation day (23 June). Values of 5–9 kg m^{-2} are found over an area of approximately 142,000 km^2. Aged cold pools from preceding days are spread over a larger area of nearly 10^6 km^2 with at least 1 kg m^{-2}. The contour lines of the layer depth between 700 and 925 hPa in Figure 9 indicate that the southward moving air from aged cold pools can lead

to a deformation of the heat low. However, the majority of the moisture from evaporation is not yet reaching the SHL core region at the end of the simulation. For the second case the total amount of moisture released over 4 days is smaller with an area of approximately 621,000 km^2 above 1 kg m^{-2}. For both cases the affected area is impressive, but the seemingly small integrated water vapor signals need to be seen relative to typical Saharan values. For both cases, Q_{ev} values between 5 and 9 kg m^{-2} occur where total CWV ranges from 16 to 41 kg m^{-2}. Averaged over this area, evaporated rain accounts for approximately one fifth of the total CWV. A version of Figure 9 with percentage of CWV rather than kg m^{-2} is included in the supporting information (Figure S9).

4.5. Modification of Surface Radiation Balance

As discussed in section 4.4, cold pools from convection over the Atlas Mountains transport a significant amount of moisture into the SHL. Increasing low-level water vapor in turn has been proposed to have a warming effect [*Evan et al.*, 2015], especially at nighttime. Here we therefore analyze differences in long-wave radiation between the control and no-cold-pool runs concentrating on 00 UTC in the first simulation night for both cases. Although cold pools are usually related to significant dust uplift, this aspect is here not taken into account.

The 2 m temperature in the region of the cold pool tends to be higher than in the surrounding desert (Figures S10a and S10b). This at first sight counterintuitive result has two main explanations. First, the cold pool is covered by clouds (Figures S11a and S11b) and therefore experiences less radiative cooling than the surrounding desert. Second, the enhanced turbulence within the cold pool and especially at its leading edge [e.g., *Sun et al.*, 2002] mixes relatively warmer air from above the nocturnal inversion downward [*Knippertz et al.*, 2007]. There are no upper air observations available to verify this, but model output shows a very sharp surface inversion for both cases (Figures S10 and S12), limited to the lowest two model layers (approximately 0–89 m above ground). For the first case, the residual layer above is well mixed with potential temperatures around 317 K (Figure S12a). This near-surface inversion gets broken up by the cold pool, leading to increased temperatures at the surface. From the second layer upward, however, the cold pool is colder than its surrounding as expected (Figures S10e, S10f, S7a, and S7e), which is mainly due to its formation through evaporative cooling. Temperature differences between the control and no-cold-pool runs (Figures 10a and 10b) show that closer to the mountains, the effect of evaporative cooling dominates leading to colder temperatures with the cold pool included, while farther into the desert the breaking up of the surface inversion dominates leading to warmer temperatures. For both cases the surface temperature signals show a very close structural match to those in upwelling long-wave radiation (LW_{up}), which reaches positive values as high as 40 Wm^{-2} near the leading edge (Figures 10c and 10d).

An additional effect is the formation of arc clouds above the leading edge (Figures S11c and S11d), which reduces radiative cooling in the control run for both cases, as reflected by positive differences in downwelling long-wave radiation (LW_{down}) relative to the no-cold-pool experiments (Figures 10e and 10f). For the second case, this cloud formation is well visible in infrared satellite images (Figure 7f) but seems to be somewhat overestimated by WRF for the first case (cf. Figure 5f).

The differences in net radiation balance (Figures 10g and 10h) are negative for most of the cold-pool region except for only a few grid points along the leading edge. That indicates that the involved dynamics effectively remove energy from the lower troposphere by increasing radiative cooling, particularly through the heating of the surface due to vertical mixing, which in turn radiates this energy into space. Only parts of the increased LW_{up} are reflected back by additionally generated arc clouds. However, these nighttime conditions are not long lived, as the discussed mechanism only works as long as the cold pool propagates farther into an area with a surface inversion, which is usually destroyed by solar heating shortly after sunrise. As also pointed out by *Bou Karam et al.* [2014], the propagation at daytime is slowed down due to vertical mixing, which decreases the density difference to the environment.

What remains after the development of the daytime convective boundary layer is the additional moisture from rain evaporation, which usually gets mixed vertically much deeper than the original cold pool. The Saharan PBL can reach up to 550 hPa [*Garcia-Carreras et al.*, 2015]. Accordingly, the mixing ratio gets reduced, but the vertically integrated amount, which is relevant for LW_{down}, remains unchanged. The tracer variable Q_{ev} (see section 3.3) can be used to show the radiative effect of the cold pools independent of their dynamics. To do this, WRF runs were started at 00 UTC after subtracting the tracer from the full field: $Q_{modified} = Q_v - Q_{ev}$. The model was then integrated over one time step only for both original and modified water vapor fields.

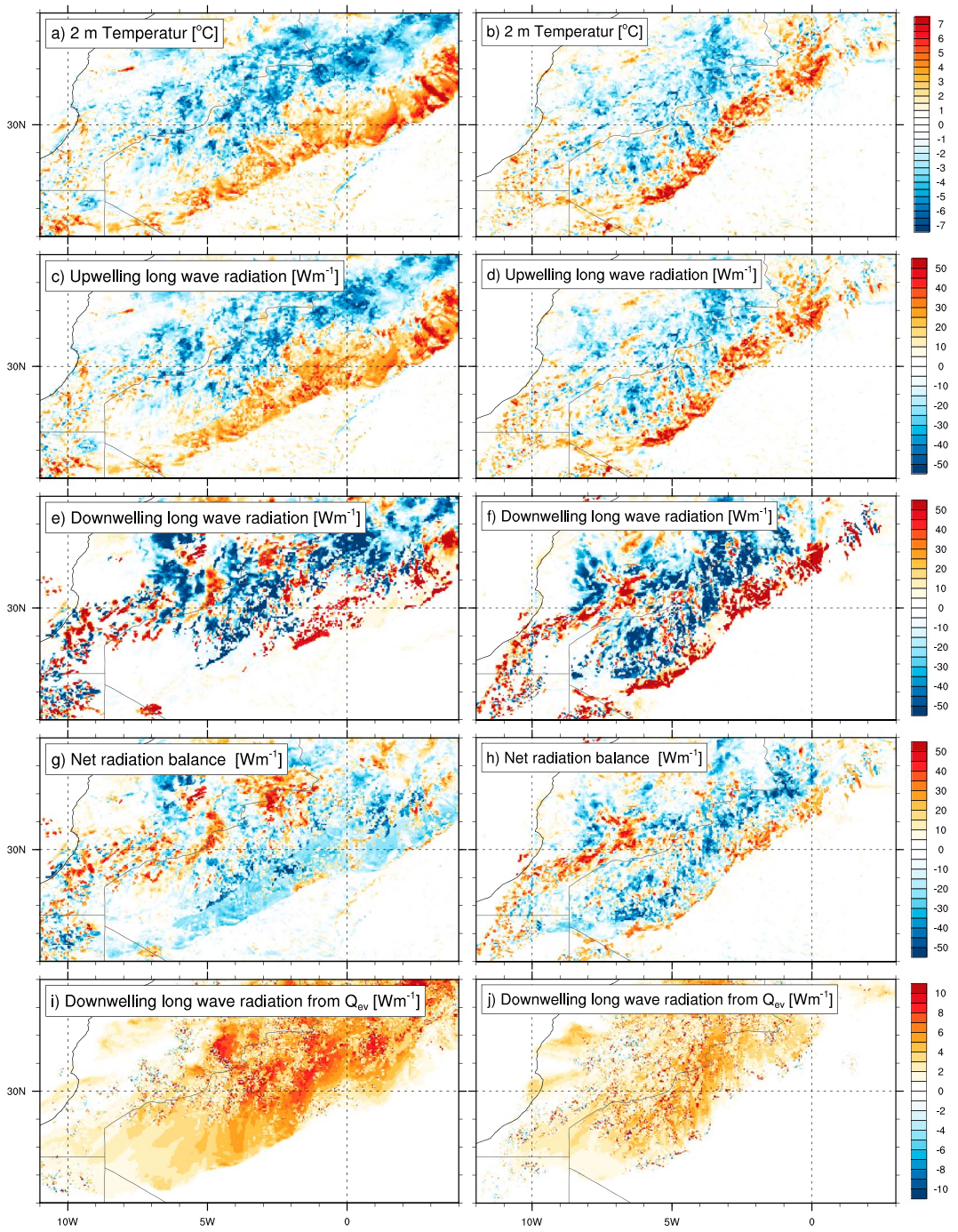


Figure 10. Impact of cold pool on radiation balance and surface temperature; shown are differences (control run—no-cold pool). (a, c, e, g, i) Case 2011-06-20 and (b, d, f, h, j) case 2012-06-27. For both cases, initialization time +24 h (00 UTC of first night).

Figures 10i and 10j show that the contribution of the additional moisture to the nighttime radiation balance is 5–10 Wm^{-2}. Despite integration over one time step only, changes in cloud fraction occur at some grid points, leading to larger differences locally. During the following day, the magnitude of the forcing is slightly reduced, as Q_{ev} is spread horizontally over a larger area. For the first case, the area with more than 1 Wm^{-2} is increased from 0.8×10^6 to 1.2×10^6 km^2 from 00 to 12 UTC. In the same time the area with more than 5 Wm^{-2} decreases slightly from 229,000 to 197,000 km^2. The development for the second case is comparable, but the affected area is smaller (only 36,200 km^2 above 5 Wm^{-2} at 12 UTC). At daytime, the short-wave part of the

radiation balance needs to be accounted for, too. The additional moisture has a negative impact on the same order of magnitude but does not fully cancel out the long-wave signal (Figure S13). A linear regression analysis between Q_{ev} and downwelling components of the radiation balance from both cases yields a 00 UTC value of +1.27 Wkg^{-1} in LW_{down} and 12 UTC values of +2.11 Wkg^{-1} in LW_{down} versus −1.88 Wkg^{-1} in downwelling short-wave radiation (SW_{down}). The latter values are in very good agreement with observations (+2.0 Wkg^{-1} in LW_{down} versus −1.8 Wkg^{-1} in SW_{down}) from the Fennec supersite BBM [*Marsham et al.*, 2015].

For both cases, the contribution of Q_{ev} to the radiation balance remains stable throughout the whole integration period, as deep convection on consecutive days compensate consumption of Q_{ev} through cloud and rain formation. The dynamical effects clearly dominate during the first night of a fresh cold pool, especially close to its origin. Nevertheless, this is very likely overcompensated during the following days as the moisture remains in the atmosphere. A typical value of 5 Wm^{-2} at night is likely too small to be relevant for short model runs but becomes important for reliable climate projections, as it is of the same order of magnitude as anthropogenic greenhouse-gas forcing.

4.6. Representation of Cold Pools With Low Resolution

Due to large computational costs, the horizontal resolution of 3 km used for the control runs is too fine for most regional climate projections, where typical grid spacings range from 0.22° to 0.44°. This requires the use of parameterized convection, which is known to have negative impacts on the representation of cold pools [*Marsham et al.*, 2013b]. Here we quantify this effect for the first case based on differences between the 3 km control run and model runs with 0.22° resolution and different convection schemes (Table 1). After 30 integration hours (06 UTC), the runs show significant differences in 2 m T_d to the control run and to a lesser extent to each other (Figure 11). Higher T_d in the control run between 25°N and 30°N show an underestimation of the moisture transport associated with the leading edge of the cold pool for all schemes, while differences farther north are small or even negative. The differences south of 20°N are caused by convection in the Sahel region.

The Betts-Miller-Janjic (BMJ) and Grell-Freitas (GF) schemes (Figures 11b and 11c) show particularly large deviations, while for example Tiedtke or Zhang-McFarlane (ZMF) looks surprisingly close to the control run (Figures 11f and 11g). The leading edge of the cold pool at 06 UTC is located within the box 10°W–0°W, 24°N–30°N. For the GF (Tiedtke) scheme, the root-mean-square differences (RMSD) over this box is 3.11 K (0.96 K) with a maximum bias of 7.84 K (3.88 K). This is contrary to a case study by *Reinfried et al.* [2009], in which Tiedtke underestimates an Atlas cold pool with a significantly worse performance than KF. Domain-wide RMSDs have a much smaller range from 1.89 to 2.17 K. Interestingly, using no parameterization for convection at all (Figure 11i), which is not recommended for a rather coarse grid spacing of 0.22°, leads to the smallest domain-wide RMSD of 1.75 K. While no general conclusions should be drawn from this result alone, it is in line with findings from *Marsham et al.* [2013b], *Birch et al.* [2014], and *Stein et al.* [2015] for 12 km runs and emphasizes the need for improved schemes.

Even though all parameterization schemes produce significant biases, they do not completely fail to reproduce the cold pool in agreement with work by *Reinfried et al.* [2009] and *Bou Karam et al.* [2014]. Here this aspect is further analyzed in vertical cross sections perpendicular to the leading edge, the cold pool (i.e., almost parallel to the low-level wind vector, see Figure 4c for location) in an earlier state of the simulation at 00 UTC. For these cross sections the experiment was repeated with 0.44° and 0.75° resolution, always using the Tiedtke convection scheme, which performed best in the 0.22° experiment. In addition to the leading edge, the wind distribution highlights a second interesting feature, namely, a NLLJ, somewhat south of the leading edge of the cold pool (Figure 12a). The maximum wind speed within the cold pool of 24.1 ms^{-1} is reached in an altitude of about 640 m above the surface at 28.4°N. With the first decrease in horizontal resolution to 0.22°, the leading edge of the cold pool is still well visible (Figure 12b). The maximum is somewhat smoothed to 20.4 ms^{-1} but found in the correct position. Decreasing the resolution further to 0.44° leads to more smoothing and a maximum of 17.2 ms^{-1}. This time, the location of the maximum is located about 1° farther in the north, indicating wrong timing of the event or wrong propagation speed. Also, the maximum is found about 300 m closer to the surface. At 0.75° resolution (for example used for ERA-Interim), the wind speed maximum of the cold pool is still visible but is reduced to 15.5 ms^{-1} and now significantly replaced northward to 30.2°N. The NLLJ, which is not related to the convective event, is present at all horizontal resolutions at the same location. The wind speed there is also higher in the 3 km control run but nearly

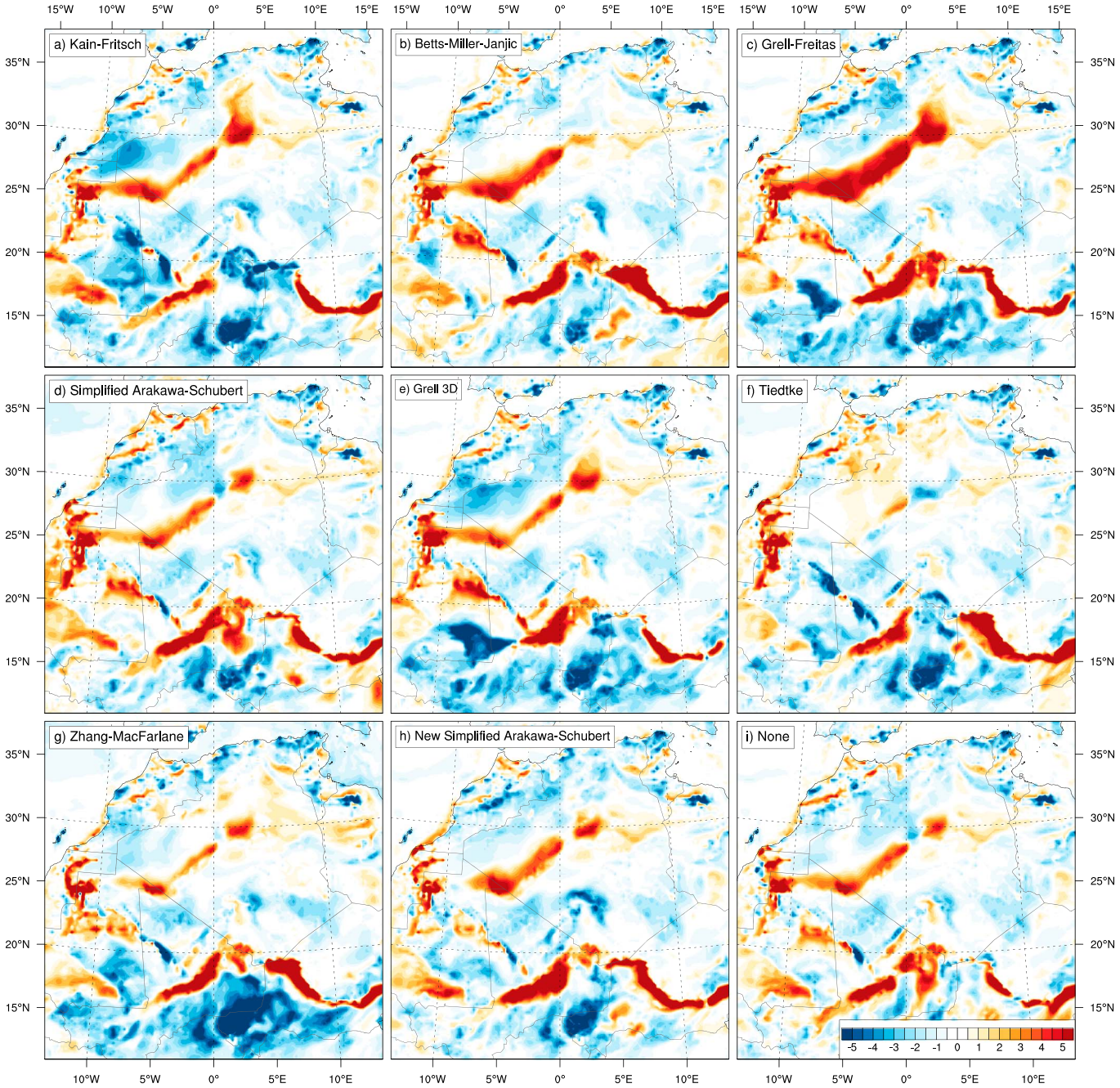


Figure 11. Differences in 2 m dew point temperature between the 3 km control run and low-resolution model runs (0.22°) with different convection parameterizations at 21 June, 06 UTC (+30 h) case 1. Positive values indicate wetter conditions in the control run.

unchanged for all lower resolutions. From these results, it can be concluded that convectively generated cold pools cause model biases that grow with decreasing horizontal resolution.

It can be expected that the parameterization schemes for deep convection have the largest impact on the development of cold pools, as the driving physical process, the evaporation of convective precipitation, is represented by this scheme. However, other schemes, e.g., the boundary layer and microphysics parameterizations, might have an influence as well, and this influence could also depend on the horizontal resolution. This was not analyzed here and should be addressed in future research on this topic along with the question of how a smoothed orography over the Atlas Mountains might influence the triggering of deep convection.

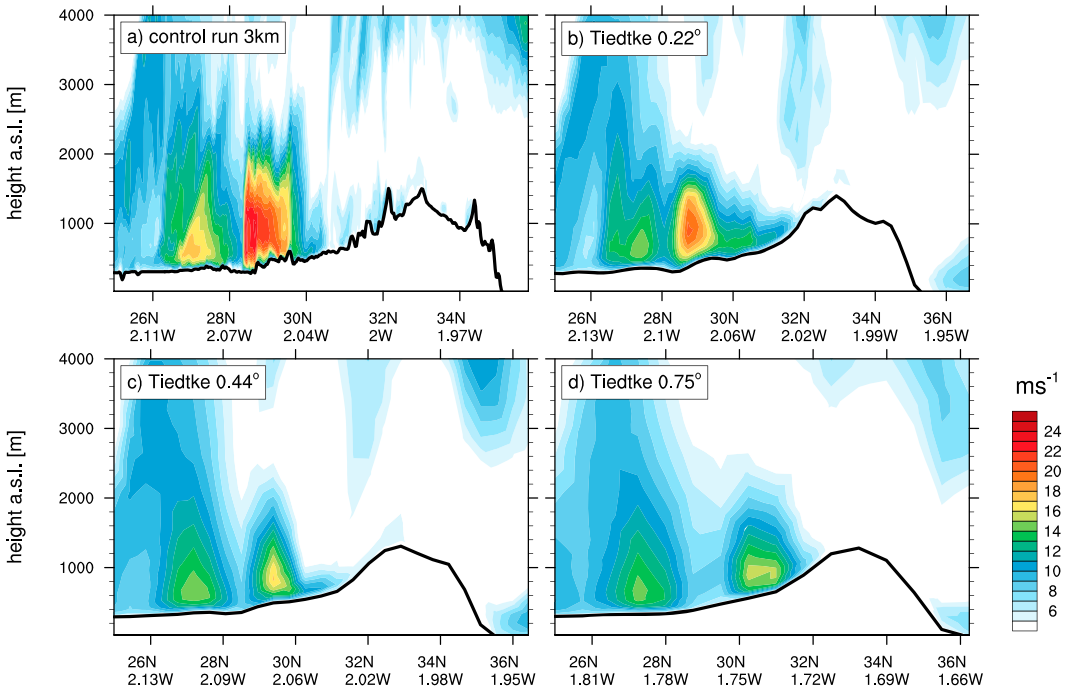


Figure 12. Vertical cross section through the cold pool of case 1 with different horizontal resolutions on 21 June at 00 UTC. (a) Control run, (b–d) using the Tiedtke scheme. Shown is the horizontal wind speed on model layers in m s^{-1}.

5. Summary and Discussion

Cold pools caused by deep moist convection over the Atlas Mountains frequently occur during the boreal summer months and often cluster into active periods of several days [*Redl et al.*, 2015]. Cold pools typically form in the afternoon and spread over hundreds of kilometers until the early morning hours. Here two cold-pool periods were selected to explore to what extent the associated changes in temperature, moisture, surface pressure, clouds, and radiation affect the strength and position of the SHL, a notoriously ill-reproduced part of the WAM system due to limited observations and often large model biases. The study is based on sensitivity experiments and a moisture tracking approach based on numerical simulations using the WRF model in convection-permitting and coarser resolutions.

The main findings from this work are as follows:

1. Surface pressure is significantly increased by 1–1.5 hPa along the northern fringes of the SHL over the length of the convective period. The response of the SHL to the changed pressure gradient is delayed by a few days.
2. A significant amount of moisture is transported into the desert by cold pools, such that about one fifth of column water vapor (CWV) comes from evaporated rain after large convective cold-pool events.
3. Effects of a very recent cold-pool event on the nighttime radiation balance are dominated by dynamic effects. The cold pool removes energy from the lower troposphere through cold air advection but more importantly by the turbulent downward transport of sensible heat to the surface and resulting increased upwelling long-wave radiation. However, arc clouds often form above the leading edge of the cold pool and reflect a part of the increased upwelling radiation back.
4. Beyond these initial effects, the additional moisture injected into the SHL becomes important due to its greenhouse gas effect. Downwelling long-wave radiation is increased by about 5 Wm^{-2} at day and night, which at daytime is partly compensated by reduced short-wave radiation.
5. The representation of convective cold-pool events deteriorates with decreasing horizontal resolution and the use of a parameterization for deep convection. Even with a relatively coarse grid spacing of 0.22°, a run without convection parameterization outperformed eight runs with different parameterization schemes. However, this should not be viewed as a recommendation not to use a parameterization at this resolution but as an illustration that commonly used schemes are related to large uncertainties.

Despite the marked impacts of cold pools at the northern fringes of the SHL, P_{sfc} in the core of the SHL is only affected after 4 to 6 days. In longer model runs, growing errors due to missing or ill-represented cold pools can be expected. These errors can cause a biased mean state of the SHL, which in turn can cause further indirect effects like weaker ventilation that may also modify convection at the fringes. The magnitude of direct effects found in this study motivates future research about long-term indirect effects. This includes the effect of the moisture injected into the SHL boundary layer. *Evan et al.* [2015] related the deepening of the SHL during the past decades and the simultaneous recovery from the Sahel drought in the 1970s and 1980s to an increasing amount of water vapor in lower levels in the SHL region. The results presented here suggest that cold-pool events from the Atlas Mountains form an important contribution to the availability of water vapor in this region. The misrepresentation of convective cold pools with low resolution and parameterized convection is possibly one of the reasons why *Evan et al.* [2015] found a too weak positive trend in Sahel precipitation for the past decades in CMIP5 models. However, the additional moisture from cold pools usually comes in combination with dust emitted at their leading edge. Both quantities are highly correlated to each other and counteract each other with respect to the radiation balance [*Marsham et al.*, 2015]. The lower simulated wind speeds found with cold pools from parameterized convection lead to a significantly underestimated dust emission [*Reinfried et al.*, 2009]. It is therefore possible that this underestimation and the related higher short-wave downwelling radiation compensates part of the effect of lower long-wave downwelling due to reduced water vapor mixing ratio.

Generally, the results presented here add to a growing body of work that helps in understanding the long-standing problem of misrepresentation of the WAM and its variability in many models and across timescales. Cold pools in the Sahel and, as shown here for the first time, from the Atlas Mountains and their insufficient representation should be the focus of future attempts to improve models for weather prediction and climate projections in northern Africa. Recently, some effects of cold pools have been added to existing parameterization schemes such as dust emission [*Pantillon et al.*, 2015] or effects on temperature and moisture [*Grandpeix and Lafore*, 2010], but these cannot fully represent possible upscale effects of cold pools on the SHL, which in turn may provide feedback on the convection itself. Improved climate projections for the WAM are only achievable if all aspects are taken into account. This also includes a proper representation of the complex Saharan boundary layer, which ultimately distributes moisture and dust on the continental scale [*Garcia-Carreras et al.*, 2015].

Acknowledgments
This work was primarily supported by the German Science Foundation (DFG) under FI 786/3-1. P.K. also acknowledges funding from ERC grant 257543 "Desert Storms." The IMPETUS station network was initially founded by the BMBF project IMPETUS (BMBF grant 01LW06001A, North Rhine-Westphalia grant 313-21200200) and was later maintained by the aforementioned DFG project. Data from the IMPETUS AWSs are available upon request from the corresponding author. The ISD station data set was obtained from NCDC (ftp://ftp.ncdc.noaa.gov/pub/data/noaa). The Fennec AWS data were obtained from the NERC Fennec project (NE/G017166/1), which developed, tested, and installed the AWS network. We would like to thank the National Meteorological Offices of Algeria and Mauritania for deploying and running the ground instrumentation for the Fennec field campaign. The model simulations were made possible through the Cologne High Efficiency Operating Platform for Sciences (CHEOPS, HPC cluster at the RRZK, University of Cologne, Cologne, Germany; http://rrzk.uni-koeln.de/cheops.html). MSG satellite data were obtained from the Earth Observation Portal (https://eoportal.eumetsat.int) and ECMWF (re-)analysis data from the Meteorological Archival and Retrieval System (MARS). Information about assimilated station data were kindly provided by Ersagun Kuscu from the ECMWF. Finally, we thank three anonymous reviewers for their comments that improved the manuscript.

References

Agusti-Panareda, A., A. Beljaars, C. Cardinali, I. Genkova, and C. Thorncroft (2010), Impacts of assimilating AMMA soundings on ECMWF analyses and forecasts, *Weather Forecasting*, *25*(4), 1142–1160, doi:10.1175/2010WAF2222370.1.

Allen, C. J. T., R. Washington, and S. Engelstaedter (2013), Dust emission and transport mechanisms in the central Sahara: Fennec ground-based observations from Bordj Badji Mokhtar, June 2011, *J. Geophys. Res. Atmos.*, *118*, 6212–6232, doi:10.1002/jgrd.50534.

Allen, C. J. T., R. Washington, and A. Saci (2015), Dust detection from ground-based observations in the summer global dust maximum: Results from Fennec 2011 and 2012 and implications for modeling and field observations, *J. Geophys. Res. Atmos.*, *120*, 897–916, doi:10.1002/2014JD022655.

Ashpole, I., and R. Washington (2013), A new high-resolution central and western Saharan summertime dust source map from automated satellite dust plume tracking, *J. Geophys. Res. Atmos.*, *118*, 6981–6995, doi:10.1002/jgrd.50554.

Birch, C. E., D. J. Parker, J. H. Marsham, D. Copsey, and L. Garcia-Carreras (2014), A seamless assessment of the role of convection in the water cycle of the West African Monsoon, *J. Geophys. Res. Atmos.*, *119*, 2890–2912, doi:10.1002/2013JD020887.

Booth, B. B. B., N. J. Dunstone, P. R. Halloran, T. Andrews, and N. Bellouin (2012), Aerosols implicated as a prime driver of twentieth-century North Atlantic climate variability, *Nature*, *484*(7393), 228–232, doi:10.1038/nature10946.

Bosilovich, M. G., F. R. Robertson, and J. Chen (2011), Global energy and water budgets in MERRA, *J. Clim.*, *24*(22), 5721–5739, doi:10.1175/2011JCLI4175.1.

Bou Karam, D., E. Williams, M. Janiga, C. Flamant, M. McGraw-Herdeg, J. Cuesta, A. Auby, and C. Thorncroft (2014), Synoptic-scale dust emissions over the Sahara Desert initiated by a moist convective cold pool in early August 2006, *Q. J. R. Meteorol. Soc.*, *140*(685), 2591–2607, doi:10.1002/qj.2326.

Brindley, H., P. Knippertz, C. Ryder, and I. Ashpole (2012), A critical evaluation of the ability of the Spinning Enhanced Visible and Infrared Imager (SEVIRI) thermal infrared red-green-blue rendering to identify dust events: Theoretical analysis, *J. Geophys. Res.*, *117*, D07201, doi:10.1029/2011JD017326.

Cook, K. H., and E. K. Vizy (2015), Detection and analysis of an amplified warming of the Sahara Desert, *J. Clim.*, *28*(16), 6560–6580, doi:10.1175/JCLI-D-14-00230.1.

Couvreux, F., F. Guichard, O. Bock, B. Campistron, J.-P. Lafore, and J.-L. Redelsperger (2010), Synoptic variability of the monsoon flux over West Africa prior to the onset, *Q. J. R. Meteorol. Soc.*, *136*(S1), 159–173, doi:10.1002/qj.473.

Dee, D. P., et al. (2011), The ERA-Interim reanalysis: Configuration and performance of the data assimilation system, *Q. J. R. Meteorol. Soc.*, *137*(656), 553–597, doi:10.1002/qj.828.

Dong, B., and R. Sutton (2015), Dominant role of greenhouse-gas forcing in the recovery of Sahel rainfall, *Nat. Clim. Chang.*, *5*, 757–760, doi:10.1038/nclimate2664.

Emmel, C., P. Knippertz, and O. Schulz (2010), Climatology of convective density currents in the southern foothills of the Atlas Mountains, *J. Geophys. Res.*, *115*, D11115, doi:10.1029/2009JD012863.

Engelstaedter, S., R. Washington, C. Flamant, D. J. Parker, C. J. T. Allen, and M. C. Todd (2015), The Saharan heat low and moisture transport pathways in the central Sahara—Multiaircraft observations and Africa-LAM evaluation, *J. Geophys. Res. Atmos.*, *120*, 4417–4442, doi:10.1002/2015JD023123.

Engerer, N. A., D. J. Stensrud, and M. C. Coniglio (2008), Surface characteristics of observed cold pools, *Mon. Weather Rev.*, *136*(12), 4839–4849, doi:10.1175/2008MWR2528.1.

Evan, A. T., D. J. Vimont, A. K. Heidinger, J. P. Kossin, and R. Bennartz (2009), The role of aerosols in the evolution of tropical North Atlantic ocean temperature anomalies, *Science*, *324*(5928), 778–781, doi:10.1126/science.1167404.

Evan, A. T., C. Flamant, C. Lavaysse, C. Kocha, and A. Saci (2015), Water vapor-forced greenhouse warming over the Sahara desert and the recent recovery from the Sahelian drought, *J. Clim.*, *28*(1), 108–123, doi:10.1175/JCLI-D-14-00039.1.

Fink, A. H., and A. Reiner (2003), Spatiotemporal variability of the relation between African easterly waves and West African squall lines in 1998 and 1999, *J. Geophys. Res.*, *108*(D11), 4332, doi:10.1029/2002JD002816.

Garcia-Carreras, L., J. H. Marsham, D. J. Parker, C. L. Bain, S. Milton, a. Saci, M. Salah-Ferroudj, B. Ouchene, and R. Washington (2013), The impact of convective cold pool outflows on model biases in the Sahara, *Geophys. Res. Lett.*, *40*, 1647–1652, doi:10.1002/grl.50239.

Garcia-Carreras, L., D. J. Parker, J. H. Marsham, P. D. Rosenberg, I. M. Brooks, A. P. Lock, F. Marenco, J. B. McQuaid, and M. Hobby (2015), The turbulent structure and diurnal growth of the Saharan atmospheric boundary layer, *J. Atmos. Sci.*, *72*(2), 693–713, doi:10.1175/JAS-D-13-0384.1.

Grams, C. M., S. C. Jones, J. H. Marsham, D. J. Parker, J. M. Haywood, and V. Heuveline (2010), The Atlantic inflow to the Saharan heat low: Observations and modelling, *Q. J. R. Meteorol. Soc.*, *136*(S1), 125–140, doi:10.1002/qj.429.

Grandpeix, J.-Y., and J.-P. Lafore (2010), A density current parameterization coupled with Emanuel's convection scheme. Part I: The models, *J. Atmos. Sci.*, *67*(4), 881–897, doi:10.1175/2009JAS3044.1.

Hobby, M., et al. (2013), The Fennec Automatic Weather Station (AWS) network: Monitoring the Saharan climate system, *J. Atmos. Ocean. Technol.*, *30*(4), 709–724, doi:10.1175/JTECH-D-12-00037.1.

Hourdin, F., et al. (2010), AMMA-model intercomparison project, *Bull. Am. Meteorol. Soc.*, *91*(1), 95–104, doi:10.1175/2009BAMS2791.1.

Jones, C., F. Giorgi, and G. Asrar (2011), The Coordinated Regional Downscaling Experiment (CORDEX): An international downscaling link to CMIP5, *CLIVAR Exchange*, *16*(56), 34–40.

Knippertz, P. (2008), Dust emissions in the West African heat trough—The role of the diurnal cycle and of extratropical disturbances, *Meteorol. Z.*, *17*(5), 553–563, doi:10.1127/0941-2948/2008/0315.

Knippertz, P., A. H. Fink, A. Reiner, and P. Speth (2003), Three late summer/early autumn cases of tropical-extratropical interactions causing precipitation in Northwest Africa, *Mon. Weather Rev.*, *131*(1), 116–135, doi:10.1175/1520-0493(2003)131<0116:TLSEAC>2.0.CO;2.

Knippertz, P., C. Deutscher, K. Kandler, T. Müller, O. Schulz, and L. Schütz (2007), Dust mobilization due to density currents in the Atlas region: Observations from the Saharan Mineral Dust Experiment 2006 field campaign, *J. Geophys. Res.*, *112*, D21109, doi:10.1029/2007JD008774.

Knippertz, P., et al. (2009), Dust mobilization and transport in the northern Sahara during SAMUM 2006—A meteorological overview, *Tellus B*, *61*(1), 12–31, doi:10.1111/j.1600-0889.2008.00380.x.

Lavaysse, C. (2015), Warming trends: Saharan desert warming, *Nat. Clim. Change*, *5*(9), 807–808, doi:10.1038/nclimate2773.

Lavaysse, C., C. Flamant, S. Janicot, D. J. Parker, J.-P. Lafore, B. Sultan, and J. Pelon (2009), Seasonal evolution of the West African heat low: A climatological perspective, *Clim. Dyn.*, *33*(2–3), 313–330, doi:10.1007/s00382-009-0553-4.

Lavaysse, C., C. Flamant, S. Janicot, and P. Knippertz (2010), Links between African easterly waves, midlatitude circulation and intraseasonal pulsations of the West African heat low, *Q. J. R. Meteorol. Soc.*, *136*(S1), 141–158, doi:10.1002/qj.555.

Lensky, I. M., and D. Rosenfeld (2008), Clouds-Aerosols-Precipitation Satellite Analysis Tool (CAPSAT), *Atmos. Chem. Phys.*, *8*(22), 6739–6753, doi:10.5194/acp-8-6739-2008.

Marsham, J. H., et al. (2013a), Meteorology and dust in the central Sahara: Observations from Fennec supersite-1 during the June 2011 Intensive Observation Period, *J. Geophys. Res. Atmos.*, *118*, 4069–4089, doi:10.1002/jgrd.50211.

Marsham, J. H., N. S. Dixon, L. Garcia-Carreras, G. M. S. Lister, D. J. Parker, P. Knippertz, and C. E. Birch (2013b), The role of moist convection in the West African monsoon system: Insights from continental-scale convection-permitting simulations, *Geophys. Res. Lett.*, *40*, 1843–1849, doi:10.1002/grl.50347.

Marsham, J. H., D. J. Parker, M. C. Todd, J. R. Banks, H. E. Brindley, L. Garcia-Carreras, A. J. Roberts, and C. L. Ryder (2015), The contrasting roles of water and dust in controlling daily variations in radiative heating of the summertime Saharan heat low, *Atmos. Chem. Phys. Discuss.*, *15*(14), 19,447–19,476, doi:10.5194/acpd-15-19447-2015.

Martin, E. R., C. Thorncroft, and B. B. B. Booth (2014), The multidecadal Atlantic SST-Sahel rainfall teleconnection in CMIP5 simulations, *J. Clim.*, *27*(2), 784–806, doi:10.1175/JCLI-D-13-00242.1.

Pantillon, F., P. Knippertz, J. Marsham, and C. Birch (2015), A parameterization of convective dust storms for models with mass-flux convection schemes, *J. Atmos. Sci.*, *72*, 2545–2561, doi:10.1175/JAS-D-14-0341.1.

Parker, D. J., R. R. Burton, A. Diongue-Niang, R. J. Ellis, M. Felton, C. M. Taylor, C. D. Thorncroft, P. Bessemoulin, and A. M. Tompkins (2005), The diurnal cycle of the West African monsoon circulation, *Q. J. R. Meteorol. Soc.*, *131*(611), 2839–2860, doi:10.1256/qj.04.52.

Parker, D. J., et al. (2008), The Amma Radiosonde Program and its implications for the future of atmospheric monitoring over Africa, *Bull. Am. Meteorol. Soc.*, *89*(7), 1015–1027, doi:10.1175/2008BAMS2436.1.

Redelsperger, J.-L., C. D. Thorncroft, A. Diedhiou, T. Lebel, D. J. Parker, and J. Polcher (2006), African Monsoon multidisciplinary analysis: An international research project and field campaign, *Bull. Am. Meteorol. Soc.*, *87*(12), 1739–1746, doi:10.1175/BAMS-87-12-1739.

Redl, R., A. H. Fink, and P. Knippertz (2015), An objective detection method for convective cold pool events and its application to Northern Africa, *Mon. Weather Rev.*, *143*(12), 5055–5072, doi:10.1175/MWR-D-15-0223.1.

Reinfried, F., I. Tegen, B. Heinold, O. Hellmuth, K. Schepanski, U. Cubasch, H. Huebener, and P. Knippertz (2009), Simulations of convectively-driven density currents in the Atlas region using a regional model: Impacts on dust emission and sensitivity to horizontal resolution and convection schemes, *J. Geophys. Res.*, *114*, D08127, doi:10.1029/2008JD010844.

Rienecker, M. M., et al. (2011), MERRA: NASA's Modern-Era Retrospective Analysis for Research and Applications, *J. Clim.*, *24*(14), 3624–3648, doi:10.1175/JCLI-D-11-00015.1.

Roberts, A. J., J. H. Marsham, and P. Knippertz (2014), Disagreements in low-level moisture between (re)analyses over summertime West Africa, *Mon. Weather Rev.*, *143*, 1193–1211, doi:10.1175/MWR-D-14-00218.1.

Robertson, F. R., M. G. Bosilovich, J. Chen, and T. L. Miller (2011), The effect of satellite observing system changes on MERRA water and energy fluxes, *J. Clim.*, *24*(20), 5197–5217, doi:10.1175/2011JCLI4227.1.

Rodriguez-Fonseca, B., et al. (2011), Interannual and decadal SST-forced responses of the West African Monsoon, *Atmos. Sci. Lett.*, *12*(1), 67–74, doi:10.1002/asl.308.

Ryder, C. L., et al. (2013), Optical properties of Saharan dust aerosol and contribution from the coarse mode as measured during the Fennec 2011 aircraft campaign, *Atmos. Chem. Phys.*, *13*(1), 303–325, doi:10.5194/acp-13-303-2013.

Sanogo, S., A. H. Fink, J. A. Omotosho, A. Ba, R. Redl, and V. Ermert (2015), Spatio-temporal characteristics of the recent rainfall recovery in West Africa, *Int. J. Climatol.*, *35*, 4589–4605, doi:10.1002/joc.4309.

Schuster, R., A. H. Fink, and P. Knippertz (2013), Formation and maintenance of nocturnal low-level stratus over the Southern West African Monsoon region during AMMA 2006, *J. Atmos. Sci.*, *70*(8), 2337–2355, doi:10.1175/JAS-D-12-0241.1.

Skamarock, W. C., J. B. Klemp, J. Dudhia, D. O. Gill, D. M. Barker, M. G. Duda, X.-Y. Huang, W. Wang, and J. G. Powers (2008), A Description of the advanced research WRF version 3, *NCAR Tech. Note, NCAR/TN–475+STR*, National Center for Atmospheric Research, Boulder, Colo.

Smith, A., N. Lott, and R. Vose (2011), The integrated surface database: Recent developments and partnerships, *Bull. Am. Meteorol. Soc.*, *92*(6), 704–708, doi:10.1175/2011BAMS3015.1.

Speth, P., M. Christoph, and B. Diekkrüger (Eds.) (2010), *Impacts of Global Change on the Hydrological Cycle in West and Northwest Africa*, Springer, Berlin.

Stein, T. H., D. J. Parker, R. J. Hogan, C. Birch, C. E. Holloway, G. Lister, J. H. Marsham, and S. J. Woolnough (2015), The representation of the West-African Monsoon vertical cloud structure in the Met Office Unified Model: An evaluation with CloudSat, *Q. J. R. Meteorol. Soc.*, *141*, 3312–3324, doi:10.1002/qj.2614.

Sun, J., S. Burns, and D. Lenschow (2002), Intermittent turbulence associated with a density current passage in the stable boundary layer, *Boundary Layer Meteorol.*, *105*(2), 199–219, doi:10.1023/A:1019969131774.

Todd, M. C., et al. (2013), Meteorological and dust aerosol conditions over the western Saharan region observed at Fennec Supersite-2 during the intensive observation period in June 2011, *J. Geophys. Res. Atmos.*, *118*, 8426–8447, doi:10.1002/jgrd.50470.

Vizy, E. K., and K. H. Cook (2009), A mechanism for African monsoon breaks: Mediterranean cold air surges, *J. Geophys. Res.*, *114*, D01104, doi:10.1029/2008JD010654.

Vizy, E. K., and K. H. Cook (2014), Impact of cold air surges on rainfall variability in the Sahel and wet African tropics: A multi-scale analysis, *Clim. Dyn.*, *43*(3), 1057–1081, doi:10.1007/s00382-013-1953-z.

Vizy, E. K., K. H. Cook, J. Crétat, and N. Neupane (2013), Projections of a wetter Sahel in the twenty-first century from global and regional models, *J. Clim.*, *26*(13), 4664–4687, doi:10.1175/JCLI-D-12-00533.1.

Wang, W., C. Bruyère, M. Duda, J. Dudhia, D. Gill, M. Kavulich, K. Keene, H.-C. Lin, J. Michalakes, S. Rizvi, and X. Zhang (2013), *WRF-ARW Version 3.5 Modeling System User's Guide*, 411 pp, Natl. Cent. for Atmos. Res., Boulder, Colo.

Washington, R., et al. (2012), Fennec—The Saharan climate system, *CLIVAR Exchange*, *17*(60), 31–33.

World Meteorological Organization (2010), *Manual on Codes, International Codes, Vol. I.1, Part A—Alphanumeric Codes, WMO-No. 306*, vol. I.1, 506 pp., World Meteorol. Organ., Geneva, Switzerland.